Title: Cyclomatrix Polyphosphazenes Frameworks (Cyclo-POPs) and the related nanomaterials: Synthesis, Assembly and Functionalisation

Authors: Chaoying Wan, Xiaobin Huang

PII: S2352-4928(16)30125-8
DOI: http://dx.doi.org/doi:10.1016/j.mtcomm.2017.02.001
Reference: MTCOMM 153

To appear in:

Received date: 23-9-2016
Revised date: 31-1-2017
Accepted date: 3-2-2017

Please cite this article as: Chaoying Wan, Xiaobin Huang, Cyclomatrix Polyphosphazenes Frameworks (Cyclo-POPs) and the related nanomaterials: Synthesis, Assembly and Functionalisation, Materials Today Communications http://dx.doi.org/10.1016/j.mtcomm.2017.02.001

Cyclomatrix Polyphosphazenes Frameworks (Cyclo-POPs) and the related nanomaterials: Synthesis, Assembly and Functionalisation

Chaoying Wan[1*], Xiaobin Huang[2*]

[1] International Institute for Nanocomposites Manufacturing (IINM), WMG, University of Warwick, CV4 7AL, UK;

[2] School of Aeronautics and Astronautics, Shanghai Jiao Tong University, Shanghai 200240, China

Email: chaoying.wan@warwick.ac.uk, xbhuang@sjtu.edu.cn

Graphical abstract

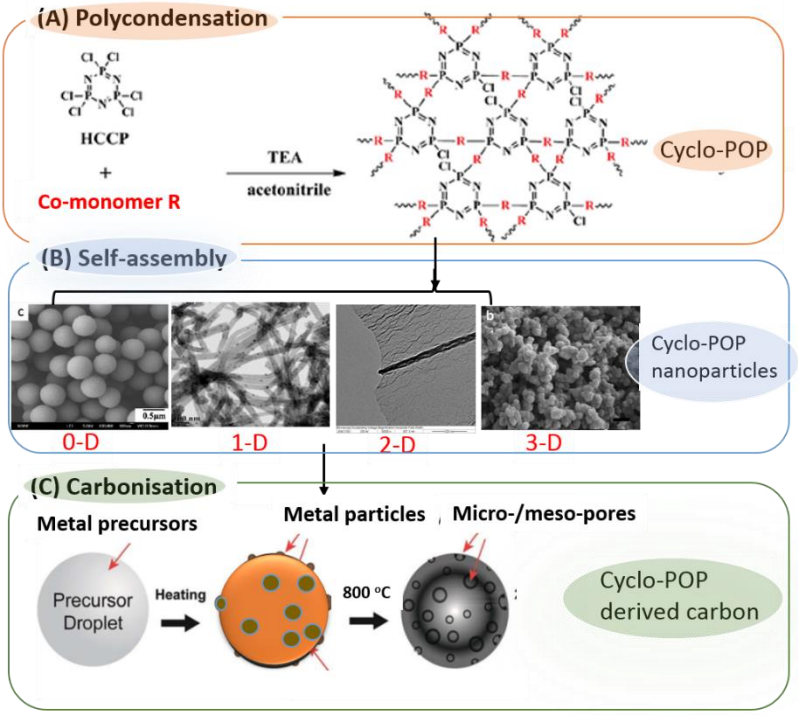

A novel type of multifunctional and robust cyclo-POP materials synthesized via a facile one-step polycondenzation and simultaneous self-assembly process.

Abstract

Poly (organophosphazene) (POP) is one of the most important inorganic polymers along with polysiloxane. The versatile phosphazene chemistry enables a wealth of functional inorganic-organic hybrid polymers with –P=N structures ranging from covalently crosslinked cyclomatrix phosphazene to linear POP copolymers. Cyclomatrix phosphazene framework materials (Cyclo-POPs) represent a

novel type of molecular composites, and can be facilely formed via a rapid one-step polycondenzation and simultaneous self-assembly process under ambient conditions, and the stereoscopic morphologies are tuneable from zero-dimension (0D) to 3D depending on the compositions and reaction conditions. The novel cyclo-POPs have shown distinctive advantages over boron-containing covalent organic framework (COFs) materials in terms of the facile and rapid synthesis and integrated functionalities. Moreover, the highly crosslinked –P=N- backbone structures are readily to be transformed into porous carbon nanomaterials with intrinsically doped heteroatoms (P, N, S, O, B, depending on the framework skeletons), which are desirable for catalysis, sensors and energy storage applications. In this article, we critically overview the rational design, synthesis and functionalisation of the cyclo-POPs materials, and their emerging applications in optoelectronics, catalysis and energy storage devices, along with the technical challenges and development perspectives.

Introduction

Poly (organophosphazenes) (POPs) are one of the most versatile classes of macromolecules and have distinguished themselves from the world of inorganic and organic polymers due to their robust and flexible inorganic-organic hybrid molecular nature and versatile post-functionalisation capacities. Polydichlorophosphazene $(PNCl_2)_n$ (**2,** shown in Fig.1) is synthesized via thermal ring-opening polymerisation of hexachlorocyclotriphosphazene (HCCP, **1**) at 250 ^oC[1,2] or living cationic polymerization of organophosphoranimines(Cl_3P=N-$SiMe_3$, **5**) at ambient temperature.[3,4,5,6] It is a landmark intermittent polymer that has led to a horizon of diverse POP derivatives and inorganic-organic polymers (**3),** by simply replacing the chlorine atoms in each monomeric unit with all kinds of nucleophiles.[7,8] This is not common in the scientific scenery of organic polymers[9]. By tailoring the side group substitutions, the properties of POPs can be well-tuned to generate radiation resistance[10], refractive index[11,12,13], ultraviolet and visible transparency[14,15,16], flame-retardancy,[17,18,19,20,21,22,23,24] biodegradability[7] and thermal stability.[25, 26] Extensive research on POPs has been carried out regarding the synthesis methodology, macromolecular design, and exploring properties and functionalities in the past decades.[25, 26]

Alternatively, cyclic phosphazenes, e.g. HCCP (**1**) with six reactive sites is a unique building block for supramolecular self-assemblies.[25, 29, 30] The ring structure of HCCP can be directly utilised to generate regio- and stereo-chemically controlled reactive intermittent (**4**) for specific functionalizations.[28,31] Recent examples are the application as core materials for precisely building of highly dense dendrimers[32] which has led to highly reusable catalysts or chemical sensors for biological applications. With different substitution groups, cyclotriphosphazene compounds can self-assemble into nanoparticles. As shown in Fig. 2ab, cyclotriphosphazene containing tryptophan ethyl esters form

nanospheres via intermolecular noncovalent π-π and CH···π interactions in a dimethylformamide (DMF)/water mixture. The cyclotriphosphazene appended with six 1,3,4-oxazodiazol containing derivatives (HPCP) self-assemble into single-crystal nano- and micro-belts in solution (Fig. 2c).[33] The shape of the nano- and microstructures can be readily controlled by varying the solvent and aging time during the self-assembly process. The overlap between the aryl units attached to the cyclotriphosphazene backbone is believed to form effective intermolecular π-π linking for crystal growth. The molecular structure of HPCP can be further modified by introducing a vinyl group to obtain hexakis-(4-(5-styryl-1,3,4-oxazodiazol-2-yl)-phenoxy)-cyclotriphosphazene (HSCP),[34] leading to the formation of micro-belts and flower-like particles through π-π interactions between neighbouring HSCP molecules (see Fig. 2d). Strong fluorescent emission arising from the side groups makes these compounds promising candidates for drug-loading carriers and tracer drug delivery. However, the synthesis procedure is complicated, and the self-assembly process takes a few days to complete.[33-34]

Cyclomatrix POPs are synthesised when HCCP reacts with dual-or tri-functional compounds (**6**, Fig.1) which results in highly crosslinked structures. Currently cyclomatrix-POPs are mainly limited to flame-retardant additives and thermoset resins due to their insolubility and poor processibility.

Our recent work on covalently crosslinked cyclomatrix polyphosphazene frameworks (cyclo-POPs) and the derived submicro-particles has overcome the above drawbacks of the bulk materials.[35,36] A series of micro/nanosized cyclo-POPs particles have been fabricated through a one-step polycondensation and simultaneous self-assembly process, which demonstrates the following characteristics: (i) the synthesis and assembly of cyclo-POPs occur in one-pot at ambient conditions; (ii) the geometry and morphology of the cyclo-POPs particles are well-tuned from 0D to 3D by simply varying the types of co-monomer and solvent, component ratio or reaction temperature; (iii) the facile synthesis of cyclo-POPs particles are readily extended to a substrate-independent coating technology. Various core-shell structured particles are obtained with the core materials ranging from magnetic (Fe_3O_4), ceramic ($BaTiO_3$, SiO_2, POSS, Si), carbon (carbon nanotube or graphene) or polymer particles (hydrophobic PS spheres and hydrophilic PLGA spheres); (iv) the surface of cyclo-POPs particles bear abundant functional groups, such as -OH, -NH_2 and –COOH originated from the co-monomers, which can be post-functionalized via polymer-grafting or doping with metal/metal salts; (v) the highly crosslinked cyclo-POPs frameworks can be directly transformed into porous carbon nanomaterials at elevated temperatures. The carbon nanomaterials have well-preserved morphology, high specific surface area, hierarchical porosity, with intrinsically doped heteroatoms such as P, S and N originated from the skeletons of the cyclo-POPs, which provide them excellent electrochemical reactivity for energy storage applications.

This article will provide a detailed review of the latest development in the synthesis, assembly and carbonization of novel cyclo-POPs based nanomaterials. The synthesis and assembly mechanism, morphology control and dimensional transition will be discussed in section 2.1. The functionalization

of cyclo-POPs by molecular structuring, encapsulation of nanoparticles and doping with metal/metal salts will be reviewed. Their applications in the fields of fluorescent sensors, adsorbents, electrolytes and catalysis will be discussed in Section 2.2. The latest research progress on hierarchical porous cyclo-POPs-derived carbon nanomaterials are introduced in Section 2.3. The perspectives and future directions will be presented in Section 3.

1. Synthesis and assembly chemistry of cyclo-POPs

Polymer nanoparticles are generally synthesized through desolvation of synthetic/natural macromolecules, or polymerization of monomers with/without template. The latter route is more feasible in tuning the geometry and morphology of polymer nanoparticles. Various polymer nanoparticles such as poly(methylmethacrylate), poly(vinylcarbazole), or polystyrene with particle sizes in the range of 50~300 nm have been formed via emulsion polymerisation, anionic polymerisation, interfacial polymerization, or controlled/living radical polymerisation.

These polymerization methods have met the challenges in the complicated synthesis routes and multi-step purification processes. Most of these synthesis methods are limited to laboratory scale, low yield and high cost. The resultant polymer particles are generally mechanically fragile and unstable under storage.[37,38] Crosslinked polymer spheres have been synthesized by precipitation polymerization by Stover's group,[39] which does not require stabilizing agents but still involves two-stage polymerization reactions.[40,41,42]

A new series of stereoscopic cyclo-POPs particles have been synthesised via the polycondensation of HCCP with organic co-monomers with dual-, or tri-functional groups through nucleophilic substitution and simultaneously assembly recently. A range of monomers have been investigated for the formation of cyclo-POPs particles and are summarised in Table 1. The rapid and facile synthesis approach offers new opportunities for large-scale production of multifunctional nanoparticles, and also overcomes the disadvantages of the poor dispersibility and processability of crosslinked cyclomatrix POP materials.

2.1 One-step polycondensation and self-assembly at ambient conditions

2.1.1 Zero-dimensional (0D) cyclo-POPs materials

A variety of commercially available and low cost compounds have been investigated and listed in Table 1. Most reactions are completed at ambient conditions within 3hrs. Among which, compound 4,4′-sulfonyldiphenol (BPS) is the most often used co-monomer to react with HCCP to form poly (cyclotriphosphazene-co-4,4′-sulfonyldiphenol) (PZS) micro/nanospheres, offering active hydroxyl groups on the sphere surface. [43, 64]

The morphology and size of cyclo-POPs particles depend on solvent polarity, co-monomer type and concentration. High polar solvents, such as acetone and acetonitrile favor spherical particles. The sphere size is determined by the initial HCCP concentration, the feed ratio of the HCCP/co-monomer and the co-monomer type. The reaction mechanism is proposed in Fig. 3.[43, 64, 65]

When HCCP and BPS are mixed in acetone or acetonitrile under ultrasonication at room temperature and an ambient atmosphere, the condensation reaction is activated by the addition of trimethylamine (TEA). Lots of primary colloids of cyclo-POP in the forms of dimers, trimers and crosslinked oligomers are formed instantly. The TEA consumes the hydrogen chloride (HCl) that is released from the condensation reaction of HCCP and BPS, and forms numerous TEA·HCl crystalline compounds. This process accelerates the nucleophilic replacement reaction between the terminal hydroxyl groups of BPS and P-Cl bonds of the HCCP, as well as provides TEA·HCl crystals as templates for the deposition of the primary oligomeric colloids. Once the agglomerate cores become stable, they are continuing to grow in size by absorbing more oligomeric species, and finally form microspheres[64,43, 65].

The polymerization and assembly process generally lasts 1~3h and yields approximately 85~95 % of products. The molar ratio of HCCP/BPS are varied between 1/3 and 1/6. The resultant PZS microspheres are 0.2 to 1.2 μm in diameter with specific surface area up to 11 m^2/g, as shown in Fig. 3c. This synthesis is rapid and catalyst-free which is much preferable over other reported reactions for producing polymer nanoparticles. [37,38,39,40,41,42]

The structures of the PZS are characterized by ^{13}C and ^{31}P CP/MAS NMR spectroscopy, as shown in **Fig.** 4a, There is no resonance of carbon at 161ppm detected from the ^{13}C CP/MAS NMR spectrum, suggesting that all phenolic hydroxyl groups of BPS has reacted with HCCP. In the ^{31}P NMR spectrum, two resonance signals appear at 32 and 19 ppm, indicating the presence of structural units -N=P(-$(OPh)_2$)-and –N=P(-OPh)(-Cl)-, which can be attributed to the incomplete chemical structure of the spherical cores. The element analysis results of PZS show P (12%), S (10%), N (5.1%), Cl (6%), and C (43%).[64] The residual Cl atoms indicates that not all of the P-Cl groups participate in the reaction due to the steric hindrance effect of the highly crosslinked structures. The PZS spheres are mainly formed by agglomeration of the oligomeric clusters, therefore generally amorphous (Fig. 4c).

The polarity and solubility parameter of the solvent affect the morphology and size of PZS. [66] The three-dimensional Hansen Solubility Parameters (HSP)[67] of the solution is related to the cohesive energy density of the solvents and polymers and indicates the affinity of a solute to a solvent. $\delta_t^2 = \delta_d^2+\delta_p^2+\delta_h^2$, where δ_t is total Hidebrand parameter, δ_d, δ_p and δ_h is the dispersion, polar, and hydrogen bond component. The polar parameter δ_p is the key polymer-solvent interactions index. PZS tends to form spherical particles in high polar solvents such as acetonitrile and acetone (δ_p=9.43), as shown in Fig. 5. The addition of non-polar toluene to acetone reduces the value of δ_p, and induces the spherical to fibrous transformation when δ_p reaches 7.43. More fibres continuously form until completely uniform nanofibers with a 60 nm outer diameter dominate in solutions at δ_p =2.43. This morphology transition is related to the solubility of the primary oligomer colloids and TEA·HCl crystals.

The TEA·HCl crystals are soluble in polar solvents such as water, acetone and acetonitrile, therefore the newly formed oligomers tend to aggregate together in spherical clusters, and precipitate directly out of the solvent. For lower polar solvents, such as THF and toluene, the TEA·HCl crystals dissolve slowly, allowing the oligomers to absorb onto the needle-like crystal surface before it is dissolved. The crystals can be dissolved and washed away during the final purification step, which leaves hollow tubular polymer particles. For linear co-monomers, the good solubility of the monomers prolong the polymerisation and precipitation process.[48] The addition of a poor solvent (e.g. water) to an organic solvent, such as acetonitrile, can facilitate the aggregation of oligomers to form polymeric clusters at above a low critical solubility parameter. This further demonstrates the templating effect of TEA·HCl crystals as discussed above and the critical role of the solvent polarity in controlling the morphology of the CPFs nanostructures.

The functionality of cyclo-POPs can be tuned by selecting co-monomers with different functional groups. Fluorinated micro/nano-spheres are formed through the polymerization of HCCP and (3,5-ditrifluoromethyl) phenylhydroquinone (6F-PH) in acetonitrile under ultrasonication[49]. Superhydrophobic PZAFs microspheres are formed with 4,4'-(hexafluoroisopropylidene)diphenol (BPAF),[68] where approximately 25.9 at% of fluorine atoms are detected by XPS from the surface and the water contact angle is 157 ± 1.5^{o} (Fig.7). The superhydrophobic PZAFs microspheres are promising materials for self-cleaning coatings with high thermal stability (>380^{o}C) and chemical durability.

Crosslinked polymer microspheres with surface functional groups such as carbonyl, hydroxyl and amino groups have found important applications in covalently binding antibodies, drug delivery and catalyst carriers.[48,45] Crosslinked microspheres bearing surface amino groups were formed by using 4,4′-diaminodiphenyl ether (ODA)[44] or branched polyethylenimine (bPEI) [27] as co-monomers (Fig.8). The particle size, surface hydrophilicity, crosslinking degree, and thermal stability can be tailored by varying the molar ratio of HCCP with the co-monomer.

To explore the bio-applications of cyclo-POPs, amino acid esters with diamine are used as an alternative to aromatic monomers, and successfully form poly(amino acid ester) nanospheres with flexible amino acid ester segments.[48] The reaction is conducted in a mixture solvent of acetonitrile and water. With L-cystine methyl ester (CysM) as a nucleophilic monomer and feed ratio of HCCP/CysM=1/3, the sphere size increases with an increase in HCCP concentration. As shown by gel permeation chromatography (GPC) in **Fig.** 9a, two new broad peaks of M_n=2655 and M_n=1341 indicate the increase of the size of HCCP molecules due to the replacement of its chlorines by CysM. As shown in **Fig.** 9bc, the product is a mixture of oligomers composed of substituted monomers and dimers in the initial stage of reaction. With the addition of water, the solubility of the oligomers decreases and larger clusters start to form.

The growing polymer spheres become stable when the solubility parameter of the acetonitrile/water reaches 18.2 cal $^{0.5}$ cm$^{-1.5}$, with a yield of 78.6%, as shown in **Fig.** 6. Similar phenomenon is found in other solvent systems, such as acetone, alcohol and tetrahydrofuran (THF). In this regard, water changes the solubility parameter of the solvent system, triggering the self-assembly and crosslinking of oligomers.

2.1.2 One-dimensional (1D) cyclo-POP materials

1D nanostructured materials in the form of fiber, rod, belt and tube can offer large aspect ratio and high specific surface area that benefit the optical, electrical and mechanical reinforcement properties. Polymer nanofibers are generally fabricated using templating-synthesis, elecrospinning, self-assembly or phase separation methods. In contrast, hybrid cyclo-POPs fibrous particles can be directly synthesised via the one-step and self-templating method at mild conditions, which offers a novel and cost-effective approach for producing nanomaterials.

Nanotubular PZSs are preferably formed in THF under ultrasonication[35]. As shown in **Fig.** 10d, the highly crosslinked PZS nanotubes are open-ended, with 5~10 nm in inner diameter, 30~60 nm in outer diameter and 1~2 μm in length, with a yield of 92%.

The polymerisation and assembly process have been monitored by TEM.[59] In the initial stage, spherical black dots of about 10-50 nm in diameter and grey 'rod-like' TEA·HCl crystals of 100 nm in length form in solution (see **Fig.** 10a). The structural features of phosphazene, sulfone, phenylene, and P-O-Ph have been detected in the black dots by FTIR, which are ascribed to the PZS oligomers. The oligomers continuously precipitate on the surface of the TEA·HCl until fully cover the crystals to form a core-shell structure (**Fig.** 10b). The TEA·HCl crystals can be washed away with water and left hollow tubular PZSs with inner diameter of 10 nm (**Fig.** 10d). Stable nanotubes and nanofibers can be formed at a ratio HCCP/BPS=1/3 mol. Only gel-like curds are formed when molar ratios are between 1/4 and 1/5.5. Soluble small molecules instead of polymers are obtained when the molar ratio is less than 1/1 or more than 1/6. Therefore, the molar ratio of HCCP and BPS affects the formation of nanotubes or nanofibres.[59]

PZS nanotubes with closed ends are obtained when the reaction is under untrasonication at 40 ^{o}C for 24h. The average size of the nanotubes are 20~30 nm in inner diameter and 100~150 nm in outer diameter, and a few micrometers in length[36, 69, 57]. The measured Brunauer-Emmett-Teller (BET) specific surface area is approximately 60 m^2/g corresponding to a total pore volume of 0.21 cm^3/g. A typical IV type curve is obtained in N_2 adsorption-desorption isotherm measurement, indicating the presence of a mixed mesoporous and microporous structure. It is suggested that the aggregation of the primary colloids forms internal pores due to the different sizes. The removal of the inner TEA·HCl nanocrystals with water at the later stage also indicates the porous nature of the nanotubes.[69] Such

porous yet covalent-crosslinked polymer nanotubes, are promising candidates for the applications including controlled drug-delivery, absorbents, nanoreactors or catalyst carriers. In addition, the high thermal stability of the PZS nanotubes (~500 °C) clearly outperforms other self-assembled block copolymer nanotubes.[70]

2.1.2 Two-dimensional (2D) cyclo-POP materials

The extension of polymer topology to 2D architectures brings unique features such as the well-defined pores with precise shape and size, high structural tunability and low density, and offers immense technological opportunities, such as molecular sieve membranes[71], catalysts[72] and optoelectronics.[73]

Following our successful synthesis of spherical and tubular cyclo-POP based nanoparticles, self-standing crystalline 2D cyclo-POP nanosheets are created by utilizing the polycondensation of HCCP and melamine, namely PPM.[62] The synthesis is carried out in DMF under ultrasonication at room temperature. The as-obtained microspherical PPM with diameter of 1~2 μm (**Fig.** 11a) starts to swell in aqueous solution under ultrasonication, and continues to exfoliate into multiple layers until fully disintegrate into nanosheets, with 0.91 nm in thickness and an interlayer spacing of about 9 nm. It is believed that the hydrogen bonding between heteroatoms (N, P in the cyclotriphosphazene and triazine segments, acting as hydrogen accepting agent) and water molecules (hydrogen donating), forms dynamic hydration layers on both sides of the PPM nanosheets[74], which results in a larger excluded volume of the hydrated nanosheets and repulsion forces between layers[75]. Therefore, the PPM tend to form a flat conformation to maximize the contact with water molecules. The dispersion in methanol or acetone do not show such disintegration behavior, which indicates that the hydrogen bonding plays a role in the structural evolution process. These results are magnificent, demonstrating the feasibility to synthesis self-standing crystalline 2D cyclo-POP nanosheets.

Furthermore, 2D microporous phosphazene-based covalent organic framework (MPCOF) are formed by the reaction of HCCP and p-phenylenediamine at a molar ratio of 1/3 in THF. [61] The reaction is carried out in an autoclave at 120 °C for 24h. The MPCOF has a specific surface area of 27.2 m^2/g, pore volume of 0.077 cm^3/g, and pore size of 1.0~2.1 nm, which is consistent with the theoretically calculated value for a 'honeycomb-like' host pore structure (1.8 nm), see **Fig.** 12. The MPCOF shows high crystallinity and relatively high heat and acid stability, as well as an excellent separation efficiency for uranium in acidic solution.[61]

Due to the nature of the fast condensation and crosslinking reaction, the formation of self-standing cyclo-POP frameworks is extremely challenging. The simultaneous assembly results in mono-dispersed nanoparticles instead of isolated molecular frameworks. The resultant nanoparticles are generally amorphous due to the lack of regularity and periodicity over the long range dimensions. The above

pioneered research on 2D cyclo-POP sheets has shed light on the feasibility of self-standing crystalline P-N molecular framework materials, which will lead to novel exciting materials in the near future.

2.1.4 Three-dimensional (3D) cyclo-POP materials

3D porous covalent electron-rich organonitridic frameworks (PECONFs) are synthesised from polycondensation reaction of 3,3′-diaminobenzidine (DAB) and HCCP in dimethylsulphoxide (DMSO)[63], see **Fig.** 13, where the DAB acts as the electron-rich aromatic building block due to its four amino groups and HCCP is used as the nitridic building unit. The PECONFs are obtained as monoliths composed with spherical particles, the moderate intergrowth of the spheres produces macropores among the spheres. The hierarchical porous structure of PECONFs enable them to adsorb high amounts of CO_2 up to 3.5 mmol/g at 1atm and 273K, high isosteric heat of adsorption and high selectivity for CO_2 over N_2. The high adsorption for methane and high selectivity of CH_4 over N_2 is due to the Lewis acid-base interactions between the electron poor CO_2 and the electron-rich sorbent. The reactivity of the unique porous structure is comparable to metal-organic frameworks (MOFs), but it is metal-free. The high thermal and chemical stability of the PECONFs are obviously advantageous over MOFs. The synthesis is much easier and cost-effective as compared to those methods for COFs.

In summary, HCCP is a unique building block for synthesis of –P=N containing covalently crosslinked cyclo-POP framework materials. The simultaneous assembly raises the challenges in obtaining isolated crystalline framework materials. The assembled cyclo-POP particles are well-tuned in size and morphology by varying the types of solvent and co-monomer as well as reaction conditions. The cyclo-POP with reactive surfaces provide a versatile platform for post-functionalization, and the highly crosslinked structure enables further carbonisation for heteroatom-doped carbon nanomaterials, which will be discussed in the following sections.

2.1 Functionalisation

Cyclo-POPs can be functionalized via bottom-up or post-synthesis approaches. The former is to using functional building block to construct cyclo-POPs frameworks. For example, superhydrophobic cyclo-POPs are synthesised by using fluoreal containing co-monomers for self-clean coatings[65]; intrinsically fluorescent cyclo-POPs are formed with fluorophores. The latter is to attach functional moieties by reacting with the surface groups of cyclo-POPs,[76,44] or by doping of metal or metal salts. The fast and facile polymerization enables excellent coating ability of cyclo-POPs by directly encapsulation of other surface or particles, such as silver nanowire[77,78,79] Fe_3O_4 [80], graphene[81] and carbon nanotubes (CNTs)[76]. These unique features facilely improve the dispersibility and stability of the nanoparticles, moreover, offer additional functional surface for post-functionalisation.[82,83,84]

2.2.1 Fluorescent cyclo-POPs -based nanosensors

Fluorescence quenching-based chemical detection is regarded as a convenient and cost-effective method for detection of highly explosive nitroaromatic compounds such as 2,4,6-trinitrotoluene (TNT), 2,4-dinitrotoluene (DNT), and picric acid (PA). The fluorescence quenching is based on a mechanism that transfers electrons from electron-rich fluorophores to electron-deficient nitro compounds[85]. Electron-rich primary amine groups can strongly bind electron deficient nitroaromatics through the formation of acid-base pairing interactions and Meisenheimer complexes,[86] therefore organic amines are always introduced to the sensor system as the receptors of nitroaromatic compounds. Instead of using complex organic ligands, fluorophores or quantum dots, cyclo-POPs bearing amine groups offers a facile way for fluorescence-based nitroaromatic sensors.

Poly(cyclotriphosphazene-co-benzidine) microspheres (PCPB-MS) synthesised by the reaction between HCCP and benzidine (**Fig.** 14a),[50] are intrinsically fluorescent due to the combination of both fluorophores and organic amino ligands in the framework structure. The quenching mechanism of PA and PCPB-MS is illustrated in **Fig.** 14b. The nitroaromatic PA are adsorbed onto the microsphere surface through charge-transfer complexing interactions between the electron-deficient aromatic rings and electron-rich amino groups, which leads to highly sensitive fluorescence quenching response. PA shows quenching constant of 18- and 10-fold higher than TNT and DNT, respectively, and also much higher than the reported value of amine-capped ZnS-Mn^{2+} nanocrystals.[87] Moreover, the highly crosslinked PCPB-MS show an intrinsically high thermal stability, good photo-bleaching stability, solvent resistance and good dispersibility in both aqueous and organic solvents, which makes it highly promising for harsh environment applications.

To utilise the aggregation-induced emission (AIE) feature, a fluorescent poly(tetraphenylethylene-co-cyclotriphosphazene) (TPE-CP) hybrid are prepared through the reaction between HCCP and dihydroxytetraphenylethylene in THF[88]. The highly crosslinked TPE-CP is stable in water and organic solvents such as THF, acetonitrile, chloroform, and methanol. The AIE feature of the tetraphenylethylene residue offers the TPE-CP strong fluorescent emission property in both the THF-water suspension and solid-state. The TPE-CP is more sensitive to PA than to TNT in the fluorescence quenching detection.[88]

Small organic fluorescent molecules with a conjugated structure usually tend to aggregate at high concentrations via π–π stacking and thus result in fluorescence quenching.[89] Curcumin shows strong fluorescence emission only at low concentration (30 μg/ml) in methanol, while by forming poly(cyclotriphosphazene-co-curcumin) microspheres (PCPC-MS), strong fluorescence emission is observed at 1 mg/ml (**Fig.** 15).[56] The cyclotriphosphazene rings are nonaromatic and photochemically inert due to the presence of a break in conjugation at each phosphorus atom.[90] The design strategy is to fix the curcumin fluorophores into the cyclo-POPs framework to construct a highly cross-linked fluorescent architecture, and meanwhile isolate the curcumin moieties from concentration quenching.[55] The PCPC-MS exhibits a fluorescence quenching response towards PA with high sensitivity, efficiency, and selectivity against a number of other analytes such as 2,4,6-trinitrotoluene, 2,4-dinitrotoluene, 1,3-dinitrobenzene, 4-nitrotoluene, nitrobenzene, 4-benzoquinone, chlorobenzene, and nitromethane in

methanol (**Fig**.15c).[89,56] This indicates their remarkable ability for resisting interferences and specific recognition of PA, and provides new insights into the design and preparation of a polymer-based fluorescence chemical sensor with low toxicity and high selectivity.

The 'isolation' and 'fastening' of fluorescent moieties such as fluorescein[51], 4,5-dibromofluorescein (DBF)[54], or phloroglucino[52] by the crosslinked framework can overcome the concentration-quenching effect and improve the photobleaching properties.[50,51,55,54]

Highly cross-linked poly(tetraphenylporphyrin-co-cyclotriphosphazene) (TPP-PZS) nanoparticles are formed through the polycondensation of HCCP and 5,10,15,20-tetrakis(4-hydroxyphenyl)porphyrin (TPP-$(OH)_4$) under ultrasonication at ambient conditions.[55] Hollow TPP-PZS spheres of 246 nm are formed when the reaction is conducted in acetonitrile, while solid irregular oval particles of 672 nm are formed in acetone. As characterised by fluorescence spectroscopy, in **Fig.** 16a[55], the hollow TPP-PZS particles show a much weaker emission peak at 660 nm than those of solid particles and TPP $(OH)_4$. The solid TPP-PZS particles emit a bright red fluorescence both in powder state and in solution because the isolation of porphyrin moieties by the cyclotriphosphazene rings (**Fig.** 16c) effectively prevents the excited electrons in porphyrin rings from transferring. While in the hollow spheres, the porphyrin rings may aggregate in the form of "H-type" (face-to-face) and "J-type" (edge-to-edge) which are observed as the broadening absorption peak at 416 nm and a new peak at 447 nm in the UV-vis absorption spectra (**Fig.** 16b). As a result, the hollow particles show weak fluorescence due to the aggregation of porphyrin. The fluorescent TPP-PZS particles also have superior resistance to photobleaching, high sensitivity and selectivity to Hg^{2+} ions (**Fig.** 16d). The TPP-PZS can be readily dip-coated to other substrates to make test strips for convenient detection or monitoring of Hg^{2+} ions.

2.2.2 Adsorbents

The dyes classified as Lewis acids (electron acceptor) and Brønsted acids (proton donor) can be selectively adsorbed onto PZSs through acid-base interactions, where the lone-pair electron-containing N atoms in PZSs favour protons or cationic dyes. The absorption mechanism and the selective adsorption of different dyes by PZSs are shown in **Fig.** 17. The cationic dyes such as methylene blue (MB), bismarck brown Y (BY), neutral red (NR) and rhodamine B (RhB) can accept the electrons from the nitrogen atoms of PZSs. Protonic acid calcein (Cal) is adsorbed by PZS due to the proton transfer or Brønsted-Lowry acid-base interaction. While orange G (OG), ponceau S (PS) and methyl orange (MO) can neither accept electrons nor donate protons. [91]

The adsorption efficiency and capacity of PZS nanoparticles for cationic RhB[92] and MB[93, 94] are dependent on temperature, initial dye concentration and adsorbent dose. The adsorption equilibrium obeys the Langmuir isotherm, and the adsorption of RhB can proceed in both basic and acidic

environment, while MB prefers neutral and basic solutions or high temperature. [93] The equilibrium adsorption capacity of PZS at 25°C for RhB reaches 35.58 mg/g within 60 min, but reaches up to 69.16 mg/g within 15 min for MB, which is much faster than most other types of adsorbents, see **Fig.** 18 and Table 2. The efficient adsorption of PZS may be ascribed to the presence of numerous electron-rich N, P and S atoms, the electrostatic attraction and π-π stacking interactions between PZS and MB.

Hydrophobic cyclomatrix polyphosphazene particles (PZAF) synthesised from the polycondensation of HCCP and 4,4′-(hexafluoroisopropylidene)diphenol, are also used for stabilizing liquid marbles.[53] The Ag nanoparticle-decorated PZAF particles (Ag/PZAF) are fabricated by an in situ reduction of silver nitrate onto PZAF particles. The reduction of MB in aqueous solution by sodium borohydride can be efficiently catalyzed within the catalytic liquid marbles at a large volume. The catalytic liquid marbles show good cycle performance without losing catalytic efficiency, as shown in **Fig.** 19. The enhanced catalytic activity is attributed to the uniform immobilization of Ag nanoparticles onto PZAF particles and the adsorption behaviour of PZAF particles toward MB, which provides a high catalytic surface area and effectively accelerates the mass transfer of MB to the Ag catalytic active sites. These results show that the unique function of PZAF particles is in the construction of catalytic mini-reactors.

2.2.3 Core-shell cyclo-POP nanostructures

2.2.3.1 Hollow nanostructures

Hollow cyclo-POP spheres with mesoporous shells can be formed with and without templates.[51,47,101] For example, poly(cyclotriphosphazene-co-fluorescein) nanospheres are formed by using SiO_2 nanoparticles as template, followed with removal of the SiO_2 by hydrofluoric acid.[51] Poly(cyclotriphosphazene-co-*p*-phenylenediamine) microspheres are synthesized by encapsulating polymeric vesicles, and then washed with water to leave hollow spheres.[101]

Poly(cyclotriphosphazene-co-phloroglucinol) (PCTP) microspheres are firstly synthesised from the polycondensation of HCCP and phloroglucinol in acetonitrile, and further treated with acetone under ultrasonication. The uniformly hollow bowl-shaped microspheres with shell thickness of 120 nm are observed in Fig.20.[102] It is suggested that the permeation of acetone destroys the hydrogen bonds between the oligomers, creating cavities inside the microspheres and eventually leads to the 'half-bowl' shape. With BPS as the crosslinker, hollow PZS spheres are also obtained after refluxing with water.[65] These results indicate that the inner core may have a lower crosslink density than the outlayer of the spheres. The hollow structure is promising for functional micro-reactor applications for catalysis and biomedical devices.

2.2.3.2 Encapsulation of nanoparticles

The rapid and facile synthesis protocols of cyclo-POPs offers them excellent coating ability onto diverse

substrates. The cyclo-POP coated metal nanowires can not only protect the metal surface from oxidation or corrosion[79, 103], but also provide a reactive surface for post-functionalization due to the abundant surface functional groups of cyclo-POPs, as discussed in Section 2.1. The sheath thickness can be controlled by vary the molar ratio of core materials to monomers. In the case of silver nanowire@PZS coaxial nanocables (**Fig.** 21), the surface energy of PZS (4.1×10^{-2} J m^{-2})[35] is much lower than that of silver nanowire (7.2 J m^{-2})[104], therefore the PZS clusters tend to wrap onto the silver surface until form a homogeneous shell. Such a wrapping process can be carried out at room temperature in the absence of any surfactant or capping agent.

Hydrophilic superparamagnetic Fe_3O_4 nanoparticles are coated by PZS in the same way.[105] The nanohybrids show negligible cytotoxicity as the PZS layer slowly degrades into less toxic forms such as 4,4′-sulfonyldiphenol, phosphate and ammonia at neutral or acid atmosphere. Considering their excellent water dispersibility, colloidal and chemical stability, magnetic manipulation, and magnetic resonance imaging (MRI) properties, the Fe_3O_4@ PZS core-shell nanohybrids are promising in MRI diagnosis applications. Fe_3O_4@ PZS@ Au[80] and Fe_3O_4@SiO_2@ PZS[106] hybrid core-shell particles can be formed by subsequently coatings (Fig.22a-c). The room-temperature magnetization curves are shown in **Fig.** 22d-e. The saturation magnetization (Ms) values of bare Fe_3O_4, Fe_3O_4@SiO_2 and Fe_3O_4@SiO_2@ PZS microspheres are 57.8, 17.9, and 6.2 emu/g, respectively, and all the samples are essentially superparamagnetic with negligible hysteresis. The hybrid nanoparticles with PZS coatings exhibit enhanced solvent resistance and water dispersion, which brings more opportunities for biotechnology applications.

Various non-covalent and covalent approaches have been developed for surface functionalization of carbon nanoparticles, such as CNTs or graphene, which have poor dispersibility in solvents and polymers due to their chemically-inert surfaces. The surface activation methods generally involve harsh acid-oxidation, wet-chemistry grafting or mechanochemistry that require large amounts of organic solvent, tedious purification processes, low yield and high cost, as well as inevitably introduce structural defects to the carbon lattices. The unique coating capacity of cyclo-POP offer a rapid, cost-effective and non-destructive approach for surface functionalization of carbon nanoparticles. The coating of cyclo-POP layers is mainly through non-covalent interaction, and can preserve the original carbon lattice structure and electrical properties.[107] Moreover, the cyclo-POP layer can make the carbon nanoparticles more benign to metal ions, such as Pt, Ag, to generate heterogeneous catalysts with enhanced electrocatalystic activities.[108, 109]

For example, an in situ polycondenstation reaction of HCCP and 4,4'-diaminodiphenyl ether (OD) in the presence of CNTs can introduce amine groups to pristine CNTs via a one-step process. The oligomeric colloids with low surface energy (41.46 mJ/m^2)[35] prefer to adsorb onto CNTs surface which has a higher surface energy (82.6 mJ/m^2)[110], as a result, a layer of crosslinked poly (cyclotriphosphazene-co-4,4'-diaminodiphenyl ether) (POD) are tightly assembled onto the CNT

surface through the nucleophilic replacement reaction of the active groups (NH_2, Cl) from adjacent crosslink nanoparticles.[76], the crosslinked POD shell is much stronger than other traditional non-covalent surface coatings on CNTs surface. The amount of the surface amine groups and the shell thickness can be tailored by varying the molar ratio of HCCP/ODA. Such amine-functionalised CNTs can reduce $HAuCl_4$ to Au particles in the absence of stabilizing or reducing agent. [76]

2.2.3.3 Functionalisation with metal nanoparticles or metal salts

Metal ions (such as Fe^{2+}, Ag^{+}, Co^{2+}, Ni^{2+}, Cu^{2+}, etc.)[111, 112] are readily doped to PZS nanoparticles through the coordination interactions with the nitrogen atoms in the P=N structures. Ag nanoparticles[77], or bimetallic Ag-Au nanoparticles with narrow size distribution (2~4 nm) have been deposited on the surface of PZS nanotubes via a co-reduction method, by using $AgNO_3$ and $HAuCl_4$ as noble metal precursors.[113]

The catalyst activity of metal doped PZS nanotubes can be evaluated by a model reduction reaction of 4-nitrophenol (4-NP) into 4-aminophenol (4-AP). It shows that the reduction reaction is completed within 8 min in the presence of PZS/Ag-Au nanotubes, while it takes 50 min for PZS/Ag and 55 min for PZS/Au nanoparticles. The turnover frequency (TOF), which is defined as the number of molecules formed per active site per second, is calculated to be 678.9 h^{-1} for the catalytic reduction of 4-NP by using PZS/Ag-Au NPs composites, much higher than other materials, such as Ag-Au nanoparticles (84.3 h^{-1}), [114] Graphene/Au-Pd (674.2 h^{-1}),[115] Fe_3O_4/C/Au-Ag (189.7 h^{-1}),[116] PZS/Ag (101.4 h^{-1}).[77] This indicates a synergistic electronic effect of the bimetallic nanoparticles, i.e., electrons could transfer from Ag to Au, leading to an increase in the electron density on the surface of the bimetallic PZS/Ag-Au nanoparticles, which improves the catalytic activity.[114,115].

Instead of doping Au nanoparticles to PZS, a layer of Au shell of 19 nm in thickness is formed by initial growth of gold nanoseeds on the PZS surface and subsequent continuous growth into gold nanoshells.[117] The core@shell structured PZS@Au showed strong surface plasmon resonance absorption in the near infrared region (700~1100 nm), where blood and biological tissues are nearly transparent. The PZS@Au can also effectively induce photothermal conversion under laser irradiation of 808 nm and rapidly killed tumor cells, suggesting potential application in photothermal imaging and therapies using NIR lasers. Ag and Au-Ag bimetallic nanoshells with tunable thickness can also be formed via a similar route by varying the mass ratio of metal salt to PZS.

2.2.3.4 Cyclo-POPs modified solid polymer electrolytes

Polyethylene oxide (PEO) is a well-known ionic conductive polymer, but its semi-crystalline structure restricts the ionic conductivity and flexibility. Various approaches have been explored in order to increase the ionic conductivity and lithium ion transfer number of polymer electrolytes, such as design new molecular structures[118,119,120,121] or incorporating ceramic fillers (such as TiO_2, Al_2O_3, SiO_2) to PEO.[121] The latter approach can reduce the crystallinity of PEO, and help to interact with both the anions

of the salts and PEO chains via Lewis acid-base interactions, however the incompatibility between the ceramic fillers and PEO generally leads to the deterioration of the mechanical properties.

As compared to traditional ceramic fillers, PZS particles are more compatible with PEO due to the abundant surface functional groups including hydroxyl-, amine-groups, epoxy- and chlorine atoms. The rigid hybrid structure of PZS particles tend to form a complex with anions and increase the lithium ion transference number.

PEO composite electrolytes containing 10 wt% of PZS microspheres (PZSMS) and $LiClO_4$, where the EO/Li molar ratio is fixed as 10, [122, 123] showed ionic conductivity 3.36×10^{-5} $S\cdot cm^{-1}$ at ambient temperature and 1.35×10^{-3} $S\cdot cm^{-1}$ at 80 °C, with Li^+ ion transference number of 0.34.[123] In this case, the PZSMS acts as Lewis acid sites to enhance the dissolvability of $LiClO_4$ and induce more free ions. The T_g and crystallinity of PEO are decreased with the PZSMS concentration increasing,[122] suggesting that the interfacial interactions among the hydroxyl groups of PZSMS and PEO chains hinders the crystalline of PEO. In contrast, the ionic conductivity of solid PEO electrolytes is 10^{-6} $S\cdot cm^{-1}$ at room temperature,[121] gum-like polymer electrolyte poly[bis(2-(2-methoxyethoxy)ethoxy)phosphazene] is about 10^{-5} $S\cdot cm^{-1}$.[118] The maximum working voltage of PEO/$LiClO_4$ can extend to 4.5 V versus Li, while it exceeds 4.8 V for PEO/$LiClO_4$/10%PZSMSs, indicating that PZSMSs widens the electrochemical stability window.

PZS nanotubes (PZSNTs) show the similar behavior as PZSMS in modification of PEO[124,125,126], but give slightly higher ionic conductivity and Li^+ ion transference number.[124] The maximum voltage of PEO/$LiClO_4$/10%PZSNT exceeds 5.0 V. This may be due to the higher specific surface area and porosity of PZSNT than PZSMS, [124] which facilitates the ions transport through the porous nanotube surface and increases the ion conductivity. In addition, the ClO_4^- anions could be trapped by the rigid nanotube structure, thus leads to an increased lithium ion transference number, similar to what is observed in boron-based systems and additives.[127] The PZS microspheres and nanotubes offer a new type of inorganic-organic hybrid materials for solid composite electrolytes.[122, 123,126, 124,125]

2.2.3.5 Cyclo-POPs-modified polymer composites

Carbon fibres (CF) are generally activated by acid oxidation with subsequent siliane-modification prior to incorporating to polymers. The multiple modification process only results in low content of surface polar groups. The coating of a layer of amine-capped crosslinked cyclo-POP polymer layer onto CFs has been realized through one-step polycondensation between HCCP and 4,4'-diaminodiphenyl ether.[128] The uniform polymer layer of 100~200 nm in thickness increases the surface roughness of CF, and therefore enhances the interfacial shear strength in the maleic anhydride grafted polypropylene.

PZS nanospheres[129] or nanotubes[130] bearing hydroxyl groups can also contribute to the chain extension and crosslinking reaction of polyurethane (PU) prepolymer, the synthesis route is shown in **Fig.** 23. The addition of 4 wt% of PZS nanospheres increases the T_g of PU by 12 °C, the thermal degradation temperature ($T_{d50\%}$) by 64 °C, and the contact angle of PU against water is increased from 70.58° to 268°. The tensile strength of the PU is increased from 11.4 to 21.5 MPa with an invariable elongation (460~430%) when the concentration of PZS is 1.5 wt%.[129]

Ternary nanoparticles (grahene-Fe_3O_4@PZM) are formed by the polycondensation of HCCP and 4,4'-diaminodi-phenylmethane (MDA) in the presence of graphene-Fe_3O_4 nanoplatelets.[81] It is observed that the Fe_3O_4 nanoparticles with diameters from 5 to 30 nm are evenly deposited on the graphene nanosheets, where PZM are coated on the Fe_3O_4 and GNS surface. The graphene-Fe_3O_4@PZM particles reinforced bismaleimide (BMI) composites showed 54.5% increase in impact strength with 0.8 wt% of aligned graphene-Fe_3O_4@PZM sheets. The composites has a low friction coefficient and volume wear rates under dry condition. The excellent properties of aligned graphene-Fe_3O_4@PZM/BMI composites are due to the uniform distribution and parallel alignment of the ternary particles in the BMI matrix, as well as good interfacial interactions ascribed to the PZM coating on the particle surface.

Epoxy-group modified PZSNTs have been prepared through the reaction with epichlorohydrin.[131]In the presence of 0.1 wt% of nanotubes, the epoxy composites show 77% and 25% of improvement in impact strength and tensile strength, respectively. Octamercaptopropyl polyhedral oligomeric silsesquioxane (POSS) has been successfully grafted to PZS nanotubes via a thiolene click reaction. [132] At 3 wt% of the POSS-PZS loading, the storage modulus of the reinforced epoxy composite is increased by 88%, and the T_g of the composite is 16 ^oC higher than that of unfilled resin. These enhancements are attributed to the high stiffness of POSS-PZS and the strong interfacial interactions.

2.2 Carbonization of cyclo-POP particles

The PZS nanoparticles with highly covalent-crosslinked structure and intrinsic -P-N- and S-O- bonds have demonstrated to be ideal candidates for preparation of heteroatom-doped carbon nanomaterials. The one-step polycondensation and subsequent carbonisation process are well-controllable, scalable and cost-effective, and have obvious advantages over the current carbon hybridization technologies.

The morphology of the PZS-derived carbon nanoparticles can be well-preserved during the carbonisation process in the temperature range of 700~1000°C in nitrogen.[133], and the porosity, heteroatom content and electrical conductivity can be tailored by the carbonisation conditions. The structure of the PZS-derived carbon nanofibers (CNFs) at different temperatures are characterised and shown in **Fig.** 28. In the Raman spectra, the value of intensity ratios of G band (at 1585 cm^{-1}, corresponds to the E_{2g} mode of graphite-like carbon) and D band (1340 ^oC, associated with the defects in carbon structures), can reflect the regularity of the carbon structure.[134] As shown in **Fig.** 24a, the I_D/I_G ratio of the CNFs increases slightly with the calcination temperature increases, which might be due to the in-plane C=C cracks at high temperature.[135] A broad XRD diffraction peak at 2θ=22-25^o suggests a typical turbostratic carbon structure.[136] The content of the heteroatoms (N, P, S and O) that originate from the PZS backbones decreases with an increase of the carbonization temperatures, as shown in **Fig.** 24b. The total heteroatoms content is up to 12.5 at% after carbonisation at 800 ^oC, which is typically higher than other reported heteroatom-doped graphene[135,134] or CNTs.[137] As shown in **Fig.** 24cd, the samples carbonized at 800, 900 and 1000 ^oC show type II isothermals with typical H3 hysteresis loops[134,138], indicating slit-shaped pores in the carbon structure. Mesopores of 2~4 nm with a narrow

pore size distribution are detected. Uniform mesopores benefit the transport of ions from electrolyte to the carbon materials, which is favourable to the power performance of the electrodes at high current densities. The BET surface area and pore volume of the carbon samples increase with an increase of the calcination temperature, but the heteroatom content decreases due to the decomposition of the -P-N bond at higher temperature (above 700 °C[63]).

The easy fabrication of the CPF-derived carbon nanomaterials with a hierarchical porous structure and intrinsically doped heteroatoms (N, O, P and S) make them outstanding candidates for catalysis and energy storage applications, which will be discussed as below.

2.3.1 Oxygen-reduction reaction catalysts

Pt-based catalysts are the most efficient oxygen reduction reaction (ORR) catalysts for fuel cells to date, but the high cost, scarcity and the deactivation effect highly hinder their practical applications. Heteroatom-doped carbon nanomaterials such as CNT, graphene or mesoporous carbon are promising catalyst carriers for Pt, which can synergistically promote the catalytic activity of Pt with a reduced usage. But the complex fabrication process of the heteroatom-doped carbons has raised another issue in this application.

PZS-derived heteroatom doped mesoporous carbon nanotubes combined with cobalt phosphide (Co_xP) nanoparticles have been prepared via direct carbonization of the composite of cobalt acetate and PZS nanotubes (Fig.25a).[139] The resultant Co_xP nanoparticles of 15~20 nm are distributed uniformly on the HMCNT surface (**Fig.** 25b). As characterized by XRD in **Fig.** 25d, the structure of Co_xP transfer from CoP to Co_2P as the carbonization temperature increases from 800 to 900 °C, suggesting the dependence of the crystalline phosphide phases on the carbonization temperature. **Fig.** 25c shows that the Co_xP nanoparticles are covered by 4~8 layers of graphitic carbon. The broad diffraction peak at 2θ=22~25° indicates a typical turbostratic carbon structure.[139]

As characterized by cyclic voltammogram and linear sweep voltammetry tests, the Co_xP- CNTs -1000 shows a high selectivity for ORR and a remarkable tolerance to methanol, and a higher diffusion-limiting current than Pt/C. The electron transfer number (n) for Co_xP- CNTs -1000 is 4.0 over the potential range from -0.3 to -0.8 V, indicating a predominant $4e^-$ ORR process.

A layer of PZAF can improve the CNTs dispersion in organic solvent as well as activate the surface of CNTs to allow the deposition of Pt catalysts. [140] As shown in **Fig.** 26ab, the PZAF/CNTs surface allows more Pt deposition than pristine CNTs. **Fig.** 26c shows the cyclic voltammogram of Pt/PZAF/CNTs for methanol oxidation. The peak current of the right oxidation peak of CH_3OH with the peak potential of 0.681 V achieves 143 mA mg^{-1}, is far greater than the literature value of 84.1 mA mg^{-1} obtained by the electrocatalytic oxidation of methanol using the pristine CNTs supported Pt nanoparticles.[108]

In another study, CNTs were coated with a ternary polymer shell which are formed by polycondensation of three types of monomers: amine terminated cyclophosphazene (ATCP), hexachlorocyclotriphosphazene (CP) and 2,2'-benzidinedisulfonic acid (BZD) before deposition of Pt nanoparticles and platinum-tin (Pt-Sn) nanoparticles.[109]. The ternary polymer shell is 3~5 nm in thickness, and can interact with the Pt and Pt-Sn nanoparticles through with $-SO_3H$, -NH and -O groups on the surface. The Pt-doped ternary polymer/CNT electrocatalysts exhibit higher stability, higher anodic oxidation current (26.59 mA $mg^{-1}$of Pt and 38.89 mA mg^{-1} of Pt-Sn) and lower onset potential (-0.64 V of Pt and -0.74 V of Pt-Sn) than those of Pt loaded Vulcan carbon and CNT materials, which can be ascribed to the synergistic effects among the metal nanoparticles, polymer shell and CNTs.

The above results indicate that the cylco-POP coatings play an important role in generating novel catalysts with enhanced electrocatalystic activity and stability. By coating of metal-doped cyclo-POP onto CNTs, the catalytic activity can be further enhanced due to the enhanced electrical conductivity.[141] Therefore, the synergistic effect via a unique host-guest electronic interaction between the transition metal nanoparticles and the graphitic carbon shell of the heteroatom-doped carbon is critical for the enhanced ORR catalytic activity.

2.3.2 Anode materials for supercapacitors and batteries

The current energy storage devices such as supercapacitors and batteries still meet the technical challenges of low energy density, poor rate capability and insufficient power density. These are mainly restricted by the structure and performance of the electrodes and electrolytes.[142] The cathode materials are dominated by transition metal salts due to their theoretically high capacity, which requires peusocapacitive properties of anode materials to match the cathode performance. These performance of carbon anodes depends on the surface area, porosity, electrical conductivity, heteroatom-doping and metal-doping. In comparison with the current often used carbon materials, such as active carbon[143], carbon nanofibers[144, 145], CNTs[146, 147], graphene and its derivatives[148, 149], and mesoporous carbon,[150] cyclo-POP derived mesoporous carbon nanoparticles have hierarchical porous structure, intrinsically highly doped heteroatoms (N, P, S, O) up to 23 at%[133] (Fig.24) These make it outstanding for inducing additional faradaic redox reactions and thus enhancing the pseudocapacitive performance of carbon-based electrodes.[151] The micro- and meso-porous structure can facilitate the penetration and transportation of electrolyte ions, and benefit the electrochemical performance at high current densities[148, 152-154].

Lightly packed cyclic phosphazenes were explored as anode materials for Li-ion batteries s by F.F. Steward's groups.[155] In their studies, the HCCP was substituted with mono-functional compounds and further chemically crosslinked with additional agents. The 3D network structure offers dimensional stability and porosity for the diffusion of Li ions. Due to the intrinsically electronic insulating, the cyclic phosphazenes materials were combined with 10 wt% of graphite and generated capacity of 183 mAh g^{-}

[1] after 50 cycles.[156] These anode materials require multistep synthesis and additional post-crosslinking.

The performance of PZSs derived carbon nanospheres with high heteroatom (N, P, S, O) doping, average diameter of 300 nm, high specific surface area of 875 m^2/g and hierarchical porosity are tested for Li-ion batteries in our recent work.[157] The carbon spheres obtained at 850 °C show a first discharge capacity of more than 1126 $mAh \cdot g^{-1}$ with a large irreversible capacity of about 440 $mAh \cdot g^{-1}$, reflecting the active surface that induces the decomposition of the electrolyte and the SEI formation on the anode. The as prepared carbon anode shows remarkable stability and coulombic efficiency for a long charge-discharge cycling up to 1000 cycles at 1C rate, delivering about 130 $mAh \cdot g^{-1}$. This indicates a synergetic effect between the unique porous structure, heteroatom doping and high surface area. The facile preparation and low thermal treatment process promise the porous HMCNSs low-cost anode materials with a high capacity and good cycle stability for Li-ion batteries.

The electrochemical performance of the HMCNFs-based electrodes[133] showed weight-specific capacitance (C_g) of 214.9 $F \cdot g^{-1}$ at a charge-discharge current density of 0.1 A/g, much higher than other reported CF-based electrodes with C_g ranging from 125 to 178 $F \cdot g^{-1}$.[158,159,160] The area-specific capacitances (C_{sa}) normalized to the BET surfaces area reaches 3.86 $F \cdot cm^{-2}$ for HMCNFs, which is much higher than that of carbon monoliths (0.094~0.011 $F \cdot cm^{-2}$) and reduced graphene (< 0.3 $F \cdot cm^{-2}$).[161,162] A higher carbonization temperature leads to a decrease in C_{sa} due to the reduced content of heteroatoms, but can increase the BET surface area (~ 790 m^2/g) and the content of mesoporous structures which still benefit the relatively high capacitance retention at high current densities. The capacitive retention ratio is more than 98% after 2000 cycles at high current density (5 A/g), indicating the outstanding stability of the electrodes. Therefore, the heteroatom content and specific surface area of carbon electrodes should be optimised.

The deposition of $MnO_2 \cdot nH_2O$ on PZS-derived carbon spheres[163] can help to stabilize the electrochemical properties of MnO_2 in electrolyte. The composite electrodes containing 25 wt% of the MnO_2 doped carbon spheres exhibits optimal specific capacitance of 218.2 $F \cdot g^{-1}$ [1] at 2 mV s^{-1}, and 112.4 $F \cdot g^{-1}$ at 100 $mV \cdot s^{-1}$. In comparison, a drastic reduction from 197.0 $F \cdot g^{-1}$ at 2 mV s^{-1} to only 40.7 $F \cdot g^{-1}$ at 100 $mV \cdot s^{-1}$ is observed for the pure α-$MnO_2 \cdot nH_2O$. The composite also shows high electrode-specific capacitance of 3.13 $F \cdot cm^{-2}$ and a long cycle life. The remarkable enhancement in the electrochemical performance is mainly attributed to the porous network of the composite facilitating the rapid transport of the electrolyte, and a great reduction of the equivalent series resistance.

Hollow structured PZS derived carbon nanospheres can offer higher surface utilization efficiency, shorter mass diffusion and lower transport resistance than solid carbon spheres[164-166]. We recently prepared hollow carbon spheres (HCMSs) with heteroatom-doping content as high as 11.5 at%, and a BET surface area of 2199 $m^2 \cdot g^{-1}$, the HCMSs-based electrodes show a specific capacitance of 314.6

$F \cdot g^{-1}$ at a current density of 0.2 A/g in 6 M KOH electrolyte, and high stability of 98.2% of capacity retention after 2000 cycles.[101] In comparison, hollow porous carbon spheres that derived from carbonization of porous organic frameworks[167] showed a specific capacitance of 230 $F \cdot g^{-1}$ at a current density of 0.5 $A \cdot g^{-1}$. Hollow carbon nano-cocoons produced from core/shell Fe_2O_3/carbon precursors exhibited a capacitance of 220 $F \cdot g^{-1}$ at a scan rate of 5 $mV \cdot s^{-1}$, and stability with 98% of capacity maintained after 1000 cycles[168]. The hollow carbon structure ensures good performance by increasing utilization efficiency of the surface area as well as achieving short diffusion paths for electrolyte ions.

2. Summery and Perspectives

Phosphorous-containing covalent organic frameworks (cyclo-POP) represent a novel type of porous functional hybrids along with covalent organic frameworks (COFs) and metal organic frameworks (MOFs). The cyclo-POP materials have distinguished themselves in the world of porous molecular composites in the follow aspects: (1) a library of compounds with dual- or tri-functional groups are applicable as co-monomers to react with HCCP. The morphology of cyclo-POPs are tuneable by varying the types of monomer and solvent as well as the reaction conditions; (2) cyclo-POPs are formed via a one-step polycondensation reaction at ambient conditions which is obviously advantageous over those synthesis protocols for COFs and MOFs; (3) The functionalities of the cyclo-POPs can be designed by molecular structuring by introducing functional co-monomers (such as fluorescein, fluorine, radical-containing moieties); post-functionalisation of the assembled cyclo-POP nanoparticles by polymer grafting, doping with metal/metal salts nanoparticles, or encapsulating nanoparticles; (4) the highly crosslinked cyclo-POP derived carbon nanoparticles are desirable for energy storage, due to their hierarchical porous structure, intrinsically doped heteroatoms, mechanical robustness and electro-chemical activity.

The development of high performance cyclo-POPs materials has met the following technical challenges: (i) the formation of cyclo-POP frameworks is accompanied by simultaneous assembly so that generally results in mono-dispersed nanoparticles instead of isolated molecular frameworks; (ii) The resultant cyclo-POP nanoparticles are amorphous due to the lack of regularity and periodicity over the long range dimensions; (iii) The formation mechanism is still not fully understood, while the crosslinked cyclo-POP nanoparticles are chemically stable but electronically insulating.

By carefully selecting the reactant, 2D cyclo-POP nanoporous crystalline nanosheets are emerging,[61,28,101] which demonstrates the feasibility of creating new features of self-standing P-N molecular framework materials. To facilitate the formation of self-standing cyclo-POPs, the shape-persistent building units with bifunctional groups (e.g., phenol, thiophenol, or amine) can potentially aid the confinement of in-plane polymerization and facilitate the covalent propagation of periodicity within the lateral dimension.[169,170] Alternatively, the simultaneous substitution of the two geminal

chlorines on each P atom of HCCP can potentially lead to precision control of the 2D morphology with long-range structural ordering by avoiding unnecessary crosslinking among groups.[171,172] The synthesis protocols towards self-standing cyclo-POPs are to be developed. The relationship of short- and long-range structure of cyclo-POPs under different assembly conditions needs to be investigated. The substitution and arrangement of redox-active co-monomers or conjugated oligomers[173] will afford electron-conductive or electrochemical active cyclo-POPs, although the doping of metal ions or encapsulation of carbon nanoparticles have been actively studied for these purposes. On the other hand, the self-assembled cyclo-POPs in the forms of nanospheres or nanotubes overcome the disperibility and processibility of cyclomatrix polyphosphazene bulk materials, together with the chemical stability, thermal stability and intrinsic functionalities, the development of electroactive cyclo-POP nanomaterials will be the new direction along with the development of COFs and MOFs.

Reference

1. H. N. Stokes, *Am. Chem. J.*, 1895, **17**.
2. H. R. Allcock and R. L. Kugel, *Journal of the American Chemical Society*, 1965, **87**, 4216-4217.
3. H. R. Allcock, J. M. Nelson, S. D. Reeves, C. H. Honeyman and I. Manners, *Macromolecules*, 1997, **30**, 50-56.
4. H. R. Allcock, C. A. Crane, C. T. Morrissey, J. M. Nelson, S. D. Reeves, C. H. Honeyman and I. Manners, *Macromolecules*, 1996, **29**, 7740-7747.
5. H. R. Allcock, S. D. Reeves, J. M. Nelson and I. Manners, *Macromolecules*, 2000, **33**, 3999-4007.
6. V. Blackstone, A. P. Soto and I. Manners, *Dalton Transactions*, 2008, 4363-4371.
7. S. Rothemund and I. Teasdale, *Chemical Society Reviews*, 2016, **45**, 5200-5215.
8. H. R. Allcock, K. B. Visscher and Y.-B. Kim, *Macromolecules*, 1996, **29**, 2721-2728.
9. V. Chandrasekhar and B. Murugesapandian, *Accounts of Chemical Research*, 2009, **42**, 1047-1062.
10. M. K. Kundu, G. Hatui, C. K. Das, V. Nigam and A. K. Saxena, *Polymer - Plastics Technology and Engineering*, 2015, **54**, 691-702.
11. H. R. Allcock, J. D. Bender, Y. Chang, M. McKenzie and M. M. Fone, *Chemistry of Materials*, 2003, **15**, 473-477.
12. M. Olshavsky and H. R. Allcock, *Macromolecules*, 1997, **30**, 4179-4183.
13. M. A. Olshavsky and H. R. Allcock, *Macromolecules*, 1995, **28**, 6188-6197.
14. G. A. Carriedo, F. J. García Alonso, P. Gómez Elipe, J. L. García-Alvarez, M. P. Tarazona, M. T. Rodríguez, E. Saiz, J. T. Vázquez and J. I. Padrón, *Macromolecules*, 2000, **33**, 3671-3679.
15. T. Fushimi and H. R. Allcock, *Dalton Transactions*, 2010, **39**, 5349-5355.
16. Y. N. Guo, C. Zhao, S. Z. Liu, D. Li, S. J. Wang, J. J. Qiu and C. M. Liu, *Polymer Bulletin*, 2009, **62**, 421-431.
17. G. A. Carriedo and M. L. Valenzuela, *Macromolecules*, 2010, **43**, 126-130.
18. J. N. Wang, X. Y. Su, L. Ya, W. T. Chen, F. Chen, Y. Chen and Z. P. Mao, *Journal of Donghua University (English Edition)*, 2015, **32**, 384-389.
19. K. Tao, J. Li, L. Xu, X. Zhao, L. Xue, X. Fan and Q. Yan, *Polymer Degradation and Stability*, 2011, **96**, 1248-1254.

20. T. Mayer-Gall, D. Knittel, J. S. Gutmann and K. Opwis, *ACS Applied Materials and Interfaces*, 2015, **7**, 9349-9363.
21. T. Zhang, Q. Cai, D. Z. Wu and R. G. Jin, *Journal of Applied Polymer Science*, 2005, **95**, 880-889.
22. T. Zhang and R. G. Jin, *Journal*, 2006, **11-12**, 395-398.
23. H. Liu, X. Wang and D. Wu, *Polymer Degradation and Stability*, 2015, **118**, 45-58.
24. J. Sun, Z. Yu, X. Wang and D. Wu, *ACS Sustainable Chemistry and Engineering*, 2014, **2**, 231-238.
25. M. Gleria and R. De Jaeger, *Phosphazenes: A worldwide insight*, Nova Publishers, 2004.
26. R. De Jaeger and M. Gleria, *Progress in Polymer Science*, 1998, **23**, 179-276.
27. J. Köhler, S. Kühl, H. Keul, M. Möller and A. Pich, *Journal of Polymer Science Part A: Polymer Chemistry*, 2014, **52**, 527-536.
28. S. Yeşilot and A. Uslu, *Polymer Reviews*, 2016, DOI: 10.1080/15583724.2016.1191023, 1-35.
29. X. Li, B. Li, Z. Li and S. Zhang, *RSC Advances*, 2012, **2**, 5997-6004.
30. X. Li, Z. Li, Y. Jing, B. Bing and B. Li, *Journal of Colloid and Interface Science*, 2012, **375**, 41-49.
31. G. A. Carriedo, *Journal of the Chilean Chemical Society*, 2007, **52**, 1190-1195.
32. A.-M. Caminade, A. Hameau and J.-P. Majoral, *Dalton Transactions*, 2016, **45**, 1810-1822.
33. S.-Z. Liu, X. Wu, A.-Q. Zhang, J.-J. Qiu and C.-M. Liu, *Langmuir*, 2011, **27**, 3982-3990.
34. S.-Z. Liu, J.-J. Qiu, A.-Q. Zhang and C.-M. Liu, *RSC Advances*, 2013, **3**, 7472-7478.
35. L. Zhu, Y. Xu, W. Yuan, J. Xi, X. Huang, X. Tang and S. Zheng, *Advanced Materials*, 2006, **18**, 2997-3000.
36. L. Zhu, X. Huang and X. Tang, *Macromolecular Materials and Engineering*, 2006, **291**, 714-719.
37. J. P. Rao and K. E. Geckeler, *Progress in Polymer Science*, 2011, **36**, 887-913.
38. L. A. Renna, C. J. Boyle, T. S. Gehan and D. Venkataraman, *Macromolecules*, 2015, **48**, 6353-6368.
39. K. Li and H. D. H. Stöver, *Journal of Polymer Science Part A: Polymer Chemistry*, 1993, **31**, 3257-3263.
40. D. Qi, F. Bai, X. Yang and W. Huang, *European Polymer Journal*, 2005, **41**, 2320-2328.
41. F. Bai, X. Yang and W. Huang, *European Polymer Journal*, 2006, **42**, 2088-2097.
42. F. Bai, X. Yang, R. Li, B. Huang and W. Huang, *Polymer*, 2006, **47**, 5775-5784.
43. Y. Zhu, X. Huang, W. Li, J. Fu and X. Tang, *Materials Letters*, 2008, **62**, 1389-1392.
44. P. Zhang, X. Huang, J. Fu, Y. Huang, Y. Zhu and X. Tang, *Macromolecular Chemistry and Physics*, 2009, **210**, 792-798.
45. H. Ozay and O. Ozay, *Colloids and Surfaces A: Physicochemical and Engineering Aspects*, 2014, **450**, 99-105.
46. Z. Li, G. Wang, A. Zhang, L. An and Y. Tian, *Journal of Applied Polymer Science*, 2016, **133**, n/a-n/a.
47. W. Liu, X. Huang, H. Wei, K. Chen, J. Gao and X. Tang, *Journal of Materials Chemistry*, 2011, **21**, 12964-12968.
48. Z. Huang, S. Chen, X. Lu and Q. Lu, *Chemical Communications*, 2015, **51**, 8373-8376.
49. Y. Wang, L. Shi, W. Zhang, Z. Jiang and J. Mu, *Polymer Bulletin*, 2014, **71**, 275-285.
50. W. Wei, X. Huang, K. Chen, Y. Tao and X. Tang, *RSC Advances*, 2012, **2**, 3765-3771.
51. L. Sun, T. Liu, H. Li, L. Yang, L. Meng, Q. Lu and J. Long, *ACS Applied Materials & Interfaces*, 2015, **7**, 4990-4997.
52. T. Pan, X. Huang, H. Wei, W. Wei and X. Tang, *Macromolecular Chemistry and Physics*, 2012, **213**, 1590-1595.
53. W. Wei, R. Lu, W. Ye, J. Sun, Y. Zhu, J. Luo and X. Liu, *Langmuir*, 2016, **32**, 1707-1715.
54. L. Meng, C. Xu, T. Liu, H. Li, Q. Lu and J. Long, *Polymer Chemistry*, 2015, **6**, 3155-3163.
55. Y. Hu, L. Meng and Q. Lu, *Langmuir*, 2014, **30**, 4458-4464.

56. W. Wei, R. Lu, S. Tang and X. Liu, *Journal of Materials Chemistry A*, 2015, **3**, 4604-4611.
57. J. Fu, X. Huang, Y. Huang, L. Zhu, Y. Zhu and X. Tang, *Macromolecular Materials and Engineering*, 2008, **293**, 173-177.
58. J. Fu, X. Huang, Y. Zhu, L. Zhu and X. Tang, *Macromolecular Chemistry and Physics*, 2008, **209**, 1845-1850.
59. Z. Lu, Y. Weizhong, P. Yang, T. Xiaozhen and H. Xiaobin, *Polymer International*, 2006, **55**, 1357-1360.
60. J. Fu, X. Huang, Y. Zhu, Y. Huang, L. Zhu and X. Tang, *European Polymer Journal*, 2008, **44**, 3466-3472.
61. S. Zhang, X. Zhao, B. Li, C. Bai, Y. Li, L. Wang, R. Wen, M. Zhang, L. Ma and S. Li, *Journal of Hazardous Materials*, 2016, **314**, 95-104.
62. K. Chen, C. Wan, W. Wei, X. Huang and H. Liu, *Materials Letters*, 2015, **139**, 93-97.
63. P. Mohanty, L. D. Kull and K. Landskron, *Nat Commun*, 2011, **2**, 401.
64. L. Zhu, Y. Zhu, Y. Pan, Y. Huang, X. Huang and X. Tang, *Macromolecular Reaction Engineering*, 2007, **1**, 45-52.
65. Y. Zhu, J. Fu, L. Zhu, X. Tang and X. Huang, *Polymer International*, 2008, **57**, 449-453.
66. Y. Zhu, X. Huang, J. Fu, G. Wang and X. Tang, *Materials Science and Engineering B: Solid-State Materials for Advanced Technology*, 2008, **153**, 62-65.
67. J. H. Hildebrand and R. L. Scott, *Annual Review of Physical Chemistry*, 1950, **1**, 75-92.
68. W. Wei, X. Huang, X. Zhao, P. Zhang and X. Tang, *Chemical Communications*, 2010, **46**, 487-489.
69. J. Fu, X. Huang, L. Zhu and X. Tang, *Scripta Materialia*, 2008, **58**, 1047-1049.
70. H. A. Klok and S. Lecommandoux, *Advanced Materials*, 2001, **13**, 1217-1229.
71. Y. Peng, Y. Li, Y. Ban, H. Jin, W. Jiao, X. Liu and W. Yang, *Science*, 2014, **346**, 1356-1359.
72. J. W. Colson and W. R. Dichtel, *Nat Chem*, 2013, **5**, 453-465.
73. M. Kim, J. N. Hohman, Y. Cao, K. N. Houk, H. Ma, A. K.-Y. Jen and P. S. Weiss, *Science*, 2011, **331**, 1312-1315.
74. B. Bagchi, *Chemical Reviews*, 2005, **105**, 3197-3219.
75. C.-l. Ren, R. J. Nap and I. Szleifer, *The Journal of Physical Chemistry B*, 2008, **112**, 16238-16248.
76. P. Zhang, X. Huang, J. Fu, Y. Huang and X. Tang, *Macromolecular Materials and Engineering*, 2010, **295**, 437-441.
77. M. Wang, J. Fu, D. Huang, C. Zhang and Q. Xu, *Nanoscale*, 2013, **5**, 7913-7919.
78. M. Gonsior, S. Antonijevic and I. Krossing, *Chemistry - A European Journal*, 2006, **12**, 1997-2008.
79. J. Fu, X. Huang, Y. Huang, Y. Pan, Y. Zhu and X. Tang, *The Journal of Physical Chemistry C*, 2008, **112**, 16840-16844.
80. Y. Hu, L. Meng, L. Niu and Q. Lu, *ACS Applied Materials & Interfaces*, 2013, **5**, 4586-4591.
81. C. Liu, H. Yan, Q. Lv, S. Li and S. Niu, *Carbon*, 2016, **102**, 145-153.
82. S. Duan, X. Yang, J. Mao, B. Qi, Q. Cai, H. Shen, F. Yang, X. Deng and S. Wang, *Journal of Biomedical Materials Research Part A*, 2013, **101A**, 307-317.
83. N. L. Morozowich, J. L. Nichol and H. R. Allcock, *Chemistry of Materials*, 2012, **24**, 3500-3509.
84. M. Deng, L. S. Nair, S. P. Nukavarapu, T. Jiang, W. A. Kanner, X. Li, S. G. Kumbar, A. L. Weikel, N. R. Krogman, H. R. Allcock and C. T. Laurencin, *Biomaterials*, 2010, **31**, 4898-4908.
85. J. V. Goodpaster and V. L. McGuffin, *Analytical Chemistry*, 2001, **73**, 2004-2011.
86. Y. Engel, R. Elnathan, A. Pevzner, G. Davidi, E. Flaxer and F. Patolsky, *Angewandte Chemie International Edition*, 2010, **49**, 6830-6835.
87. R. Tu, B. Liu, Z. Wang, D. Gao, F. Wang, Q. Fang and Z. Zhang, *Analytical Chemistry*, 2008, **80**, 3458-

3465.
88. X.-M. Hu, Q. Chen, D. Zhou, J. Cao, Y.-J. He and B.-H. Han, *Polymer Chemistry*, 2011, **2**, 1124-1128.
89. J. Wang, Y. Zhao, C. Dou, H. Sun, P. Xu, K. Ye, J. Zhang, S. Jiang, F. Li and Y. Wang, *The Journal of Physical Chemistry B*, 2007, **111**, 5082-5089.
90. M. Breza, *Polyhedron*, 2000, **19**, 389-397.
91. W. Wei, R. Lu, H. Xie, Y. Zhang, X. Bai, L. Gu, R. Da and X. Liu, *Journal of Materials Chemistry A*, 2015, **3**, 4314-4322.
92. M. Wang, J. Fu, Y. Zhang, Z. Chen, M. Wang, J. Zhu, W. Cui, J. Zhang and Q. Xu, *Journal of Macromolecular Science, Part A*, 2015, **52**, 105-113.
93. Z. Chen, J. Zhang, J. Fu, M. Wang, X. Wang, R. Han and Q. Xu, *Journal of Hazardous Materials*, 2014, **273**, 263-271.
94. Z. Chen, J. Fu, M. Wang, X. Wang, J. Zhang and Q. Xu, *Applied Surface Science*, 2014, **289**, 495-501.
95. Y. Yao, F. Xu, M. Chen, Z. Xu and Z. Zhu, *Bioresource Technology*, 2010, **101**, 3040-3046.
96. L. Ai, C. Zhang, F. Liao, Y. Wang, M. Li, L. Meng and J. Jiang, *Journal of Hazardous Materials*, 2011, **198**, 282-290.
97. C. D. Woolard, J. Strong and C. R. Erasmus, *Applied Geochemistry*, 2002, **17**, 1159-1164.
98. E. E. Baldez, N. F. Robaina and R. J. Cassella, *Journal of Hazardous Materials*, 2008, **159**, 580-586.
99. M. M. Ayad, A. Abu El-Nasr and J. Stejskal, *Journal of Industrial and Engineering Chemistry*, 2012, **18**, 1964-1969.
100. M. M. Ayad and A. A. El-Nasr, *The Journal of Physical Chemistry C*, 2010, **114**, 14377-14383.
101. K. Chen, X. Huang, C. Wan and H. Liu, *Electrochimica Acta*, 2016, **222**, 543-550.
102. T. Pan, X. Huang, H. Wei and X. Tang, *Macromolecular Chemistry and Physics*, 2012, **213**, 2606-2610.
103. J. Fu, J. Chen, Z. Chen, Q. Xu, X. Huang and X. Tang, *New Journal of Chemistry*, 2010, **34**, 599-602.
104. K. K. Nanda, A. Maisels, F. E. Kruis, H. Fissan and S. Stappert, *Physical Review Letters*, 2003, **91**, 106102.
105. Y. Hu, L. Meng, L. Niu and Q. Lu, *Langmuir*, 2013, **29**, 9156-9163.
106. J. Zhou, L. Meng, Q. Lu, J. Fu and X. Huang, *Chemical Communications*, 2009, DOI: 10.1039/B914394G, 6370-6372.
107. J. Fu, X. Huang, Y. Huang, J. Zhang and X. Tang, *Chemical Communications*, 2009, DOI: 10.1039/B818071G, 1049-1051.
108. B. Wu, D. Hu, Y. Kuang, B. Liu, X. Zhang and J. Chen, *Angewandte Chemie International Edition*, 2009, **48**, 4751-4754.
109. D. Prasanna and V. Selvaraj, *RSC Advances*, 2015, **5**, 98822-98833.
110. Y. C. Hong, D. H. Shin, S. C. Cho and H. S. Uhm, *Chemical Physics Letters*, 2006, **427**, 390-393.
111. X. Zhang, X. Huang and X. Tang, *Journal of Materials Chemistry*, 2009, **19**, 3281-3285.
112. T. A. Luther, F. F. Stewart, J. L. Budzien, R. A. LaViolette, W. F. Bauer, M. K. Harrup, C. W. Allen and A. Elayan, *The Journal of Physical Chemistry B*, 2003, **107**, 3168-3176.
113. Y. Yan, J. Fu, M. Wang, S. Liu, Q. Xin, Z. Chen and Q. Xu, *RSC Advances*, 2016, **6**, 24921-24928.
114. B. Xia, F. He and L. Li, *Langmuir*, 2013, **29**, 4901-4907.
115. X. Chen, Z. Cai, X. Chen and M. Oyama, *Journal of Materials Chemistry A*, 2014, **2**, 5668-5674.
116. S. Tang, S. Vongehr, Z. Zheng, H. Liu and X. Meng, *The Journal of Physical Chemistry C*, 2010, **114**, 18338-18346.
117. J. Zhou, L. Meng and Q. Lu, *Journal of Materials Chemistry*, 2010, **20**, 5493-5498.
118. C. H. Tsao, M. Ueda and P. L. Kuo, *Journal of Polymer Science, Part A: Polymer Chemistry*, 2016, **54**,

352-358.
119. Y. W. Chen-Yang, J. J. Hwang and F. H. Chang, *Macromolecules*, 1997, **30**, 3825-3831.
120. M. Grünebaum, M. M. Hiller, S. Jankowsky, S. Jeschke, B. Pohl, T. Schürmann, P. Vettikuzha, A. C. Gentschev, R. Stolina, R. Müller and H. D. Wiemhöfer, *Progress in Solid State Chemistry*, 2014, **42**, 85-105.
121. E. Quartarone and P. Mustarelli, *Chemical Society Reviews*, 2011, **40**, 2525-2540.
122. J. Zhang, X. Huang, H. Wei, J. Fu, Y. Huang and X. Tang, *Journal of Applied Electrochemistry*, 2010, **40**, 1475-1481.
123. J. Zhang, X. Huang, J. Fu, Y. Huang, W. Liu and X. Tang, *Materials Chemistry and Physics*, 2010, **121**, 511-518.
124. J. Zhang, X. Huang, H. Wei, J. Fu, W. Liu and X. Tang, *New Journal of Chemistry*, 2011, **35**, 614-621.
125. J. Zhang, X. Huang, H. Wei, J. Fu, Y. Huang and X. Tang, *Journal of Solid State Electrochemistry*, 2012, **16**, 101-107.
126. J. Zhang, X. Huang, H. Wei, J. Fu, Y. Huang and X. Tang, *Electrochimica Acta*, 2010, **55**, 5966-5974.
127. L. Li, H. Lee, H. Li, X. Yang and X. Huang, *Electrochemistry Communications*, 2009, **11**, 2296-2299.
128. X. Zhang, H. Xu and X. Fan, *RSC Advances*, 2014, **4**, 12198-12205.
129. Y. Zhou, X. Huang, X. Kang, J. Fu, Y. Zhu and X. Tang, *Macromolecular Materials and Engineering*, 2009, **294**, 605-610.
130. W. Liu, Y. Zheng, J. Li, L. Liu, X. Huang, J. Zhang, X. Kang and X. Tang, *Polymers for Advanced Technologies*, 2012, **23**, 1-7.
131. X. Gu, X. Huang, H. Wei and X. Tang, *European Polymer Journal*, 2011, **47**, 903-910.
132. S. Li, S. Qiu, B. Yu, G. Tang, W. Xing and Y. Hu, *RSC Advances*, 2016, **6**, 3025-3031.
133. K. Chen, X. Huang, C. Wan and H. Liu, *Materials Chemistry and Physics*, 2015, **164**, 85-90.
134. C. Wang, Y. Zhou, L. Sun, Q. Zhao, X. Zhang, P. Wan and J. Qiu, *The Journal of Physical Chemistry C*, 2013, **117**, 14912-14919.
135. Z. Lin, G. H. Waller, Y. Liu, M. Liu and C.-p. Wong, *Carbon*, 2013, **53**, 130-136.
136. H. Guo and Q. Gao, *Journal of Power Sources*, 2009, **186**, 551-556.
137. W. J. Lee, U. N. Maiti, J. M. Lee, J. Lim, T. H. Han and S. O. Kim, *Chemical Communications*, 2014, **50**, 6818-6830.
138. H. Zhang, V. V. Bhat, N. C. Gallego and C. I. Contescu, *ACS Applied Materials & Interfaces*, 2012, **4**, 3239-3246.
139. K. Chen, X. Huang, C. Wan and H. Liu, *Chemical Communications*, 2015, **51**, 7891-7894.
140. X. Huang, W. Wei, X. Zhao and X. Tang, *Chemical Communications*, 2010, **46**, 8848-8850.
141. K. Chen, X. Huang, C. Wan and H. Liu, *RSC Advances*, 2015, **5**, 92893-92898.
142. G. Wang, L. Zhang and J. Zhang, *Chemical Society Reviews*, 2012, **41**, 797-828.
143. J. Gamby, P. L. Taberna, P. Simon, J. F. Fauvarque and M. Chesneau, *Journal of Power Sources*, 2001, **101**, 109-116.
144. L.-F. Chen, X.-D. Zhang, H.-W. Liang, M. Kong, Q.-F. Guan, P. Chen, Z.-Y. Wu and S.-H. Yu, *ACS Nano*, 2012, **6**, 7092-7102.
145. B. Xu, F. Wu, R. Chen, G. Cao, S. Chen and Y. Yang, *Journal of Power Sources*, 2010, **195**, 2118-2124.
146. F. Picó, J. M. Rojo, M. L. Sanjuán, A. Ansón, A. M. Benito, M. A. Callejas, W. K. Maser and M. T. Martínez, *Journal of The Electrochemical Society*, 2004, **151**, A831-A837.
147. Y. Rangom, X. Tang and L. F. Nazar, *ACS Nano*, 2015, **9**, 7248-7255.
148. H. Luo, Z. Liu, L. Chao, X. Wu, X. Lei, Z. Chang and X. Sun, *Journal of Materials Chemistry A*, 2015,

3, 3667-3675.
149. M. Lee, B. H. Wee and J. D. Hong, *Advanced Energy Materials*, 2015, **5**.
150. Q. Shi, R. Zhang, Y. Lv, Y. Deng, A. A. Elzatahrya and D. Zhao, *Carbon*, 2015, **84**, 335-346.
151. D. R. Rolison, J. W. Long, J. C. Lytle, A. E. Fischer, C. P. Rhodes, T. M. McEvoy, M. E. Bourg and A. M. Lubers, *Chemical Society Reviews*, 2009, **38**, 226-252.
152. S. Dutta, A. Bhaumik and K. C. W. Wu, *Energy & Environmental Science*, 2014, **7**, 3574-3592.
153. L.-F. Chen, Z.-H. Huang, H.-W. Liang, H.-L. Gao and S.-H. Yu, *Advanced Functional Materials*, 2014, **24**, 5104-5111.
154. Z. Yu, L. Tetard, L. Zhai and J. Thomas, *Energy & Environmental Science*, 2015, **8**, 702-730.
155. K. L. Gering, F. F. Stewart, A. D. Wilson and M. L. Stone, *Journal*, 2014.
156. E. J. Dufek, M. L. Stone, D. K. Jamison, F. F. Stewart, K. L. Gering, L. M. Petkovic, A. D. Wilson, M. K. Harrup and H. W. Rollins, *Journal of Power Sources*, 2014, **267**, 347-355.
157. G. S. Pappas, S. Ferrari, X. Huang, R. Bhagat, D. M. Haddleton and C. Wan, *Materials*, 2016, **9**.
158. C. Kim and K. S. Yang, *Applied Physics Letters*, 2003, **83**, 1216-1218.
159. C. Kim, S.-H. Park, W.-J. Lee and K.-S. Yang, *Electrochimica Acta*, 2004, **50**, 877-881.
160. K. Naoi and P. Simon, *Journal of The Electrochemical Society (JES)*, 2008, **17**, 34-37.
161. A. Garcia-Gomez, G. Moreno-Fernandez, B. Lobato and T. A. Centeno, *Physical Chemistry Chemical Physics*, 2015, **17**, 15687-15690.
162. Q.-Q. Kong, C.-M. Chen, Q. Zhang, X.-H. Zhang, M.-Z. Wang and R. Cai, *The Journal of Physical Chemistry C*, 2013, **117**, 15496-15504.
163. W. Wei, X. Huang, Y. Tao, K. Chen and X. Tang, *Physical Chemistry Chemical Physics*, 2012, **14**, 5966-5972.
164. F. Ma, H. Zhao, L. Sun, Q. Li, L. Huo, T. Xia, S. Gao, G. Pang, Z. Shi and S. Feng, *Journal of Materials Chemistry*, 2012, **22**, 13464-13468.
165. X. Fang, J. Zang, X. Wang, M.-S. Zheng and N. Zheng, *Journal of Materials Chemistry A*, 2014, **2**, 6191-6197.
166. J. Han, G. Xu, B. Ding, J. Pan, H. Dou and D. R. MacFarlane, *Journal of Materials Chemistry A*, 2014, **2**, 5352-5357.
167. X. Liu, L. Zhou, Y. Zhao, L. Bian, X. Feng and Q. Pu, *ACS Applied Materials & Interfaces*, 2013, **5**, 10280-10287.
168. J. Zhang, K. Wang, S. Guo, S. Wang, Z. Liang, Z. Chen, J. Fu and Q. Xu, *ACS Applied Materials & Interfaces*, 2014, **6**, 2192-2198.
169. Z. Zheng, R. Grünker and X. Feng, *Advanced Materials*, 2016, DOI: 10.1002/adma.201506237, n/a-n/a.
170. U. Díaz and A. Corma, *Coordination Chemistry Reviews*, 2016, **311**, 85-124.
171. H. R. Allcock, D. J. Brennan and R. W. Allen, *Macromolecules*, 1985, **18**, 139-144.
172. S. Yang, J. Wang, S. Huo, M. Wang, J. Wang and B. Zhang, *Polymer Degradation and Stability*, 2016, **128**, 89-98.
173. H. Yang, S. Zhang, L. Han, Z. Zhang, Z. Xue, J. Gao, Y. Li, C. Huang, Y. Yi, H. Liu and Y. Li, *ACS Applied Materials & Interfaces*, 2016, **8**, 5366-5375.

Glossary

AIE	aggregation-induced emission
ATCP	amine terminated cyclophosphazene
BMI	bismaleimide
BET	Brunauer-Emmett-Teller
BPS	4,4′-sulfonyldiphenol
BPAF	4,4’-(hexafluoroisopropylidene)diphenol
bPEI	branched polyethylenimine
BZD	2,2’-benzidinedisulfonic acid
COFs	covalent organic frameworks
CP	hexachlorocyclotri-phosphazene
Co_xP	cobalt phosphide
CV	cyclic voltammogram
CPFs	cyclomatrix-polyphosphazenes frameworks
CysM	L-cystine methyl ester
CNTs	Carbon nanotubes
CF	Carbon fibres
DAB	3,3′-diaminobenzidine
DBF	4,5-dibromofluorescein
DDE	4,4’-diaminodiphenyl ether
DNT	2,4-dinitrotoluene
EDS	Energy-dispersive X-ray spectroscopy
EPPZTs	Epoxy-group modified PZS nanotubes
6F-PH	(3,5-ditrifluoromethyl) phenylhydroquinone
GPC	Gel Permeation Chromatography
HACP	hexakis (4-aminophenoxy) cyclotriphosphazene
HCCP	hexachlorotriphosphazene
HCl	hydrogen chloride
HSP	Hansen Solubility Parameters
LSV	Linear sweep voltammetry
MDA	4,4’-diaminodi-phenylmethane
MOFs	metal-organic frameworks
MPCOF	poly (cyclotriphosphazene-co-p-phenylenediamine)
MEEP	poly[bis(2-(2-methoxyethoxy)ethoxy)phosphazene]
MRI	magnetic resonance imaging
M-PP	maleic anhydride grafted polypropylene
ODA	4,4′-diaminodiphenyl ether
ORR	oxygen reduction reaction
PA	picric acid
PCTPF	poly(cyclotriphosphazene-co-fluorescein)
PCPB-MS	poly(cyclotriphosphazene-co-benzidine) microspheres
PPM	poly (cyclotriphosphazene-co-melamine)
PZS	poly (cyclotriphosphazene-co-4,4′-sulfonyldiphenol)
PZAF	poly (cyclotriphosphazene-co-4,4′-(hexafluoroisopropylidene)diphenol)
PCTP	Poly(cyclotriphosphazene-co-phloroglucinol)
PECONFs	Porous covalent electron-rich organonitridic frameworks
PEO	Polyethylene oxide
PZSMS	PZS microspheres
PZSNTs	PZS nanotubes
POD	poly (cyclotriphosphazene-co-4,4’-diaminodiphenyl ether)
PUA	polyurethane acrylate
POPZS	Octamercaptopropyl polyhedral oligomeric silsesquioxane grafted PZS nanotubes
RDE	rotating disk electrode
SPR	surface plasmon resonance
TEA	trimethylamine
THF	Tetrahydrofuran

TMP	trimethoprime
TNT	2,4,6-trinitrotoluene
TPE-CP	poly(tetraphenylethylene-co-cyclotriphosphazene)
TPP-PZS	poly(tetraphenylporphyrin-co-cyclotriphosphazene)
TPP-$(OH)_4$	5,10,15,20-tetrakis(4-hydroxyphenyl)porphyrin

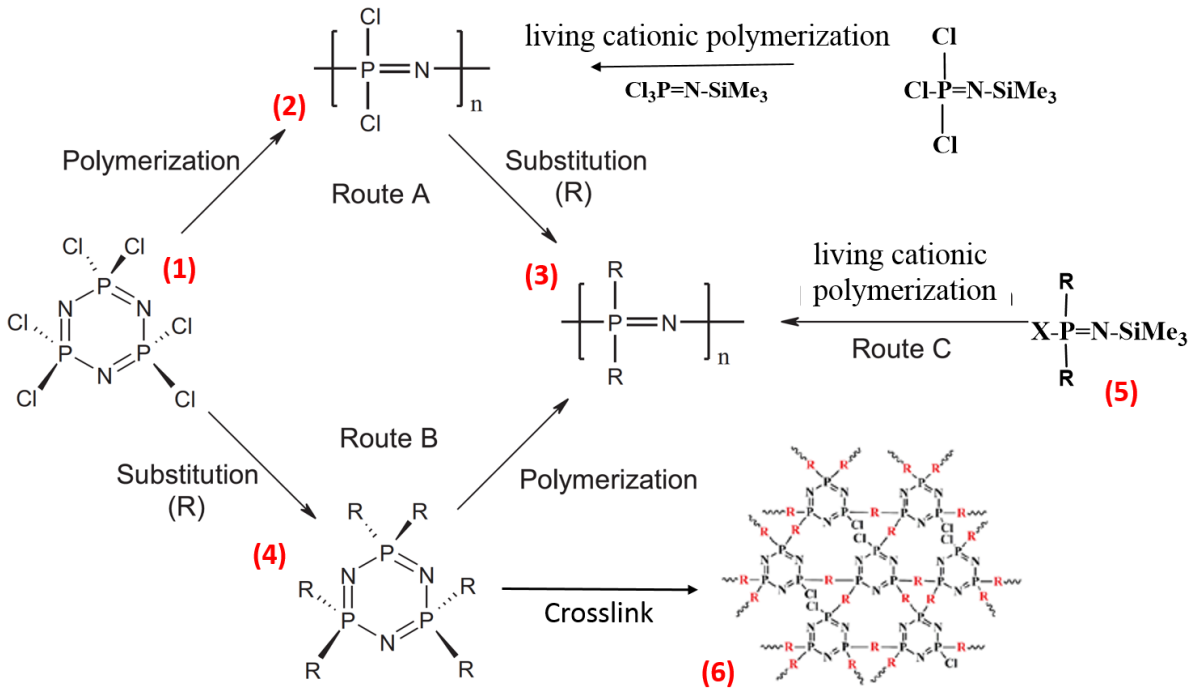

Fig. 1 Molecular structures and synthesis routes of POPs: (1) hexachlorocyclotriphosphazene (HCCP), (2) polydichlorophosphazene, (3) linear poly (organophosphazene) (POP), (4) cyclomatrix polyphosphazenes, (5) organophosphoranimines, (6) crosslinked cyclomatrix phosphazenes.[27,28].

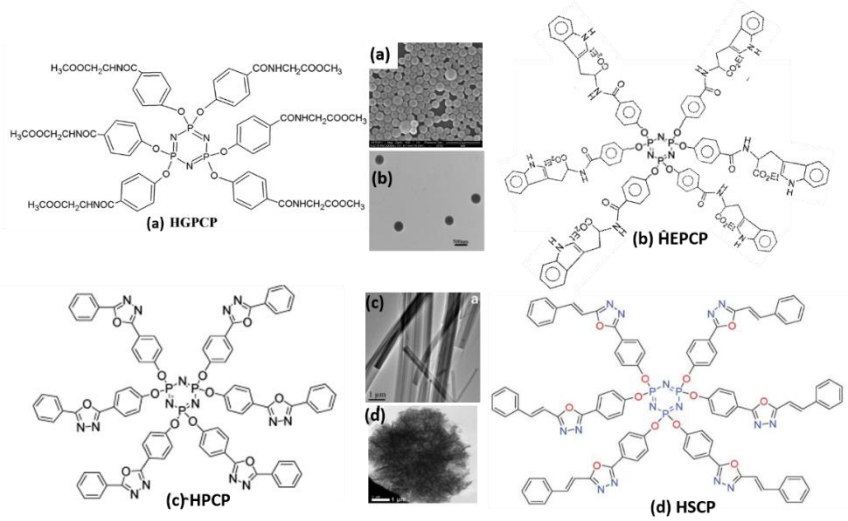

Fig. 2 Molecular structure and self-assembly morphology of cyclotriphosphazenes: (a) HGPCP nanospheres,[30] (b) HEPCP nanospheres,[29] (c) HPCP microbelts,[33] and (d) HSCP flower-like structures.[34]

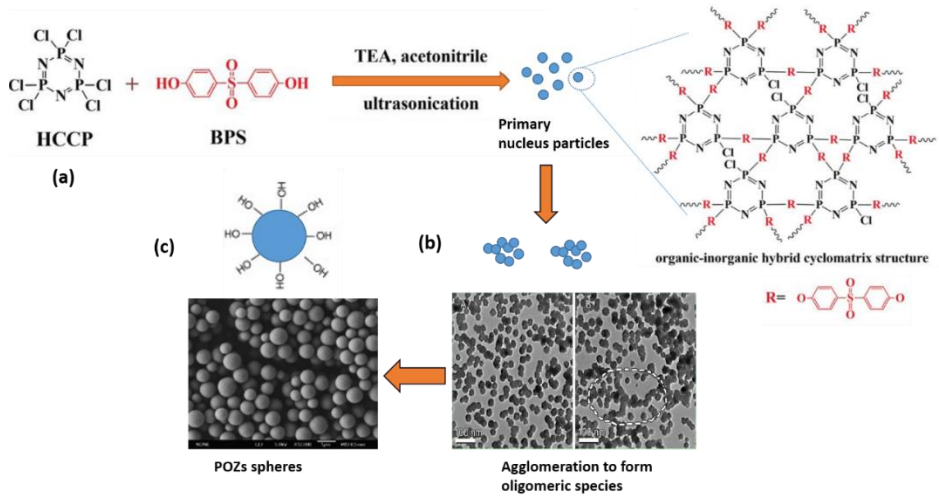

Fig. 3. (a) Reaction mechanism and self-assembly process of PZS spheres, (b) primary oligomeric colloids, and (c) PZS spheres.[43, 64, 65]

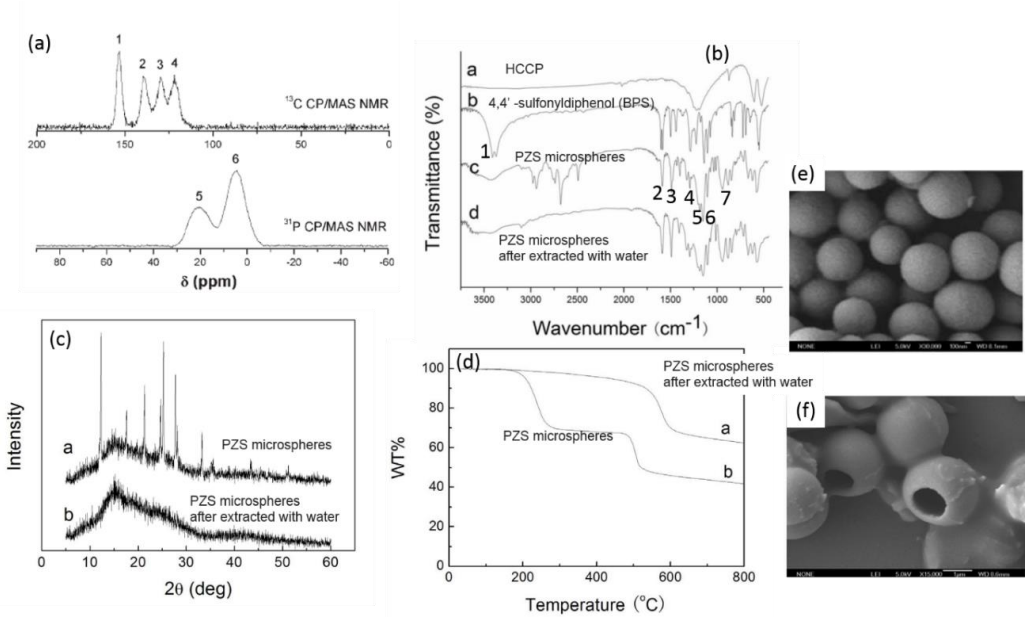

Fig. 4 (a) Solid-state ^{13}C and ^{31}P CP/MAS NMR spectrum of PZS microspheres; (b) FTIR spectrum of the monomers, PZS microspheres: assignment of spectrum of PZS microspheres: peak 1: (Ph)C-OH str, peaks 2, and 3: C=C (Ph) str, peak 4 and 6: O=S=O str, peak 5: P=N valence, peak 7: P-O-(Ph) str; and PZS microspheres refluxed in water for 2 h. [64] (c-d) XRD and TGA results of PZS microspheres before and after refluxed in water for 2h.[65] SEM of PZSs refluxed in water for (e) 0 hr and (f) 72 hr.[65]

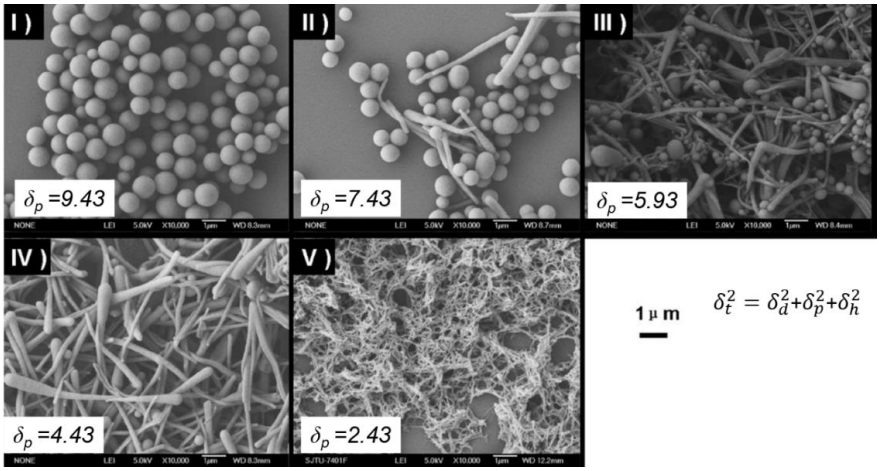

Fig. 5 SEM images of cyclo-POPs obtained from mixed solvents at different volume ratios: (I) acetone/toluene = 8/1; (II) acetone/toluene = 2/1; (III) acetone/toluene = 1/1; (IV) acetone/toluene = 1/2; (V) acetone/toluene = 1/8. [66]

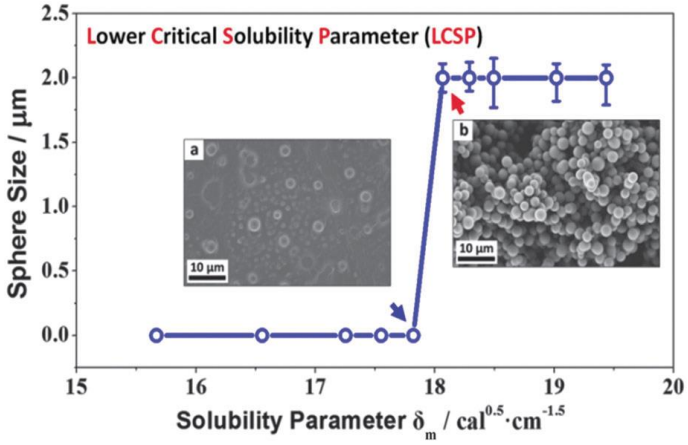

Fig. 6 The Hildebrand solubility parameter of the mixed solvent (δ_m) and its relationship with the size of PN-CysM spheres. Sphere growth did not occur at δ_m < 17.8 cal$^{0.5}$ cm$^{-1.5}$ but were formed when the δ_m >18.2 cal$^{0.5}$ cm$^{-1.5}$. The sphere size was almost constant. [48]

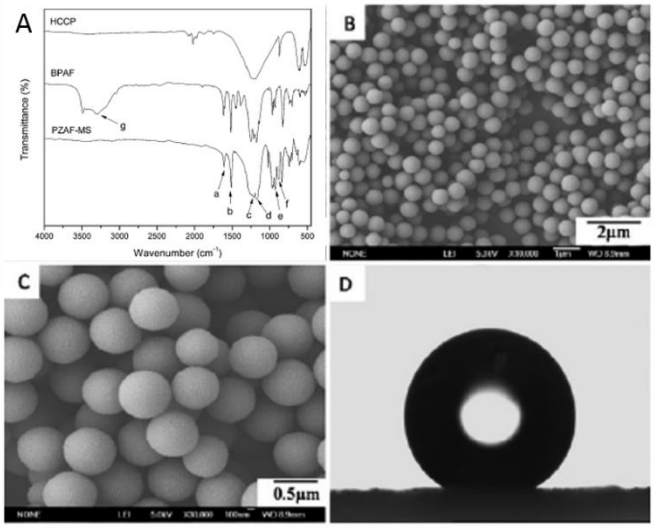

Fig. 7 (a) FTIR spectra of HCCP, BPAF and PZAF microspheres: peak a and b: CQC (Ph), peak c and d: -CF_3, peak e: P-O-(Ph), peak f: P-N, peak g: (Ph)-OH. (B-C) PZAF microspheres; (D) contact angle measurement on the PZAF coated Si wafer surface. [68]

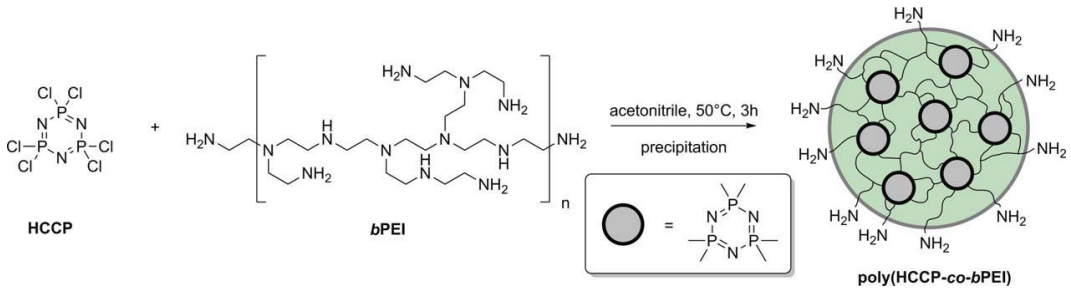

Fig. 8 Synthetic route to poly(HCCP-co-bPEI) microspheres.[27]

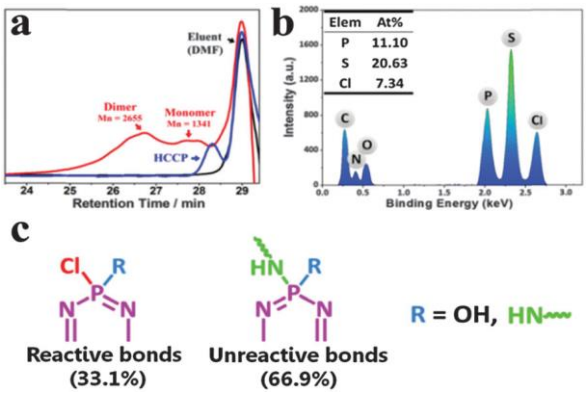

Fig. 9 Molecular structure of the oligomer. (a) GPC analysis showing the oligomers consisting of trimer (Mw = 3226), dimer (Mw = 2153) and monomer (Mw = 988). (b) EDS data of the oligomer, and its phosphorus, sulphur, and chlorine content. (c) The possible molecular formula of the trimer oligomer. [48]

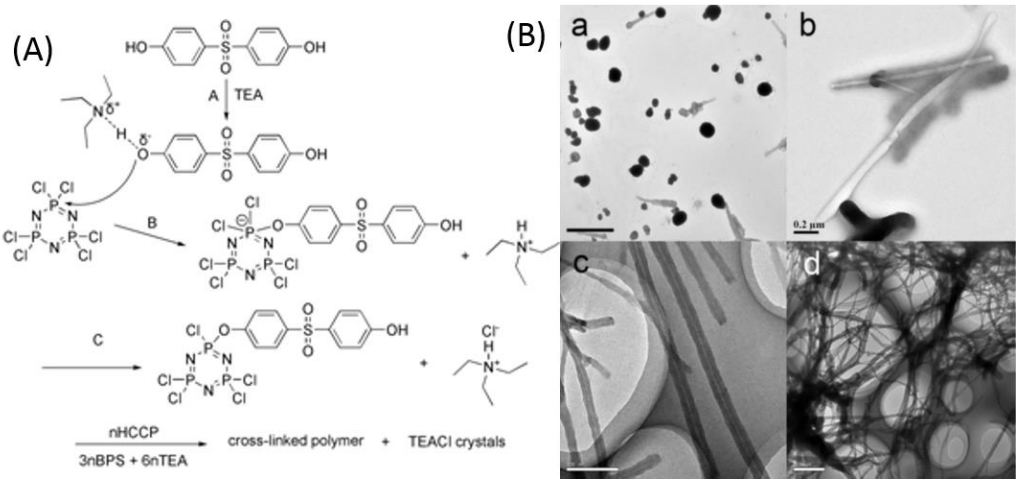

Fig. 10. (A) Condensation polymerisation of PZS nanotubes; (B) (a) generation of TEA·HCl crystals and oligomeric particles; (b) the growing TEA·HCl crystals are partially covered by the oligomeric particles; c) Core-shell structured particles form by fully wrapping of TEA·HCl crystals with

oligomers; d) flexible PZS nanotubes after removing TEA·HCl crystals with water. Scale bar: a-c) 200 nm; d) 500 nm. [59]

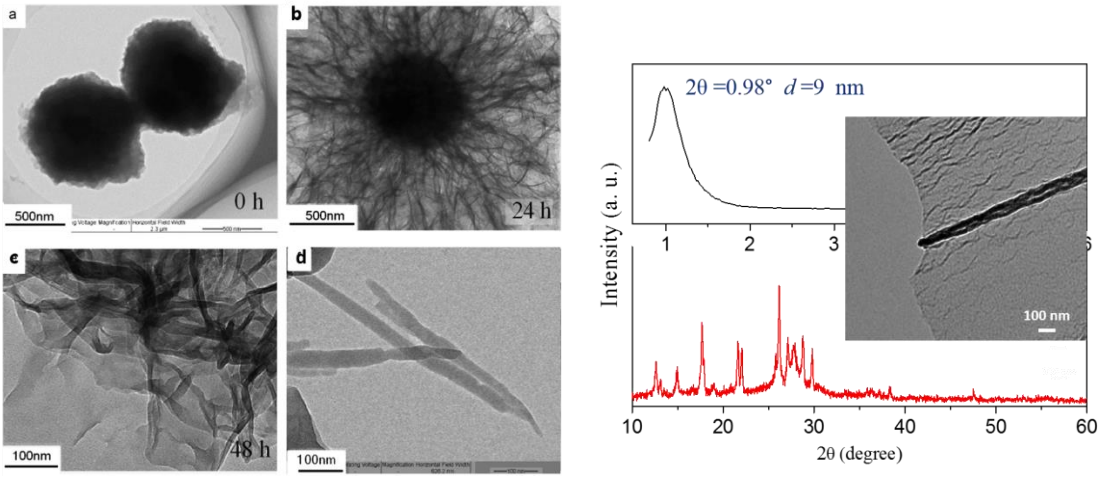

Fig. 11 Structure evolution of PPM microspheres in aqueous solution for 0, 24, and 48h and the structure characterisation.[62]

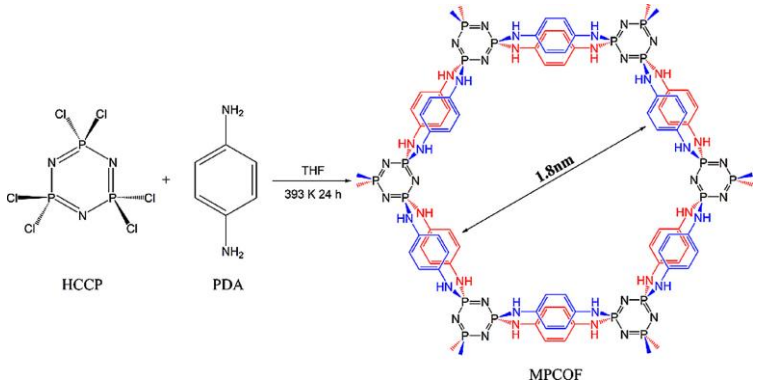

Fig. 12 Schematic illustration of the preparation of MPCOF.[61]

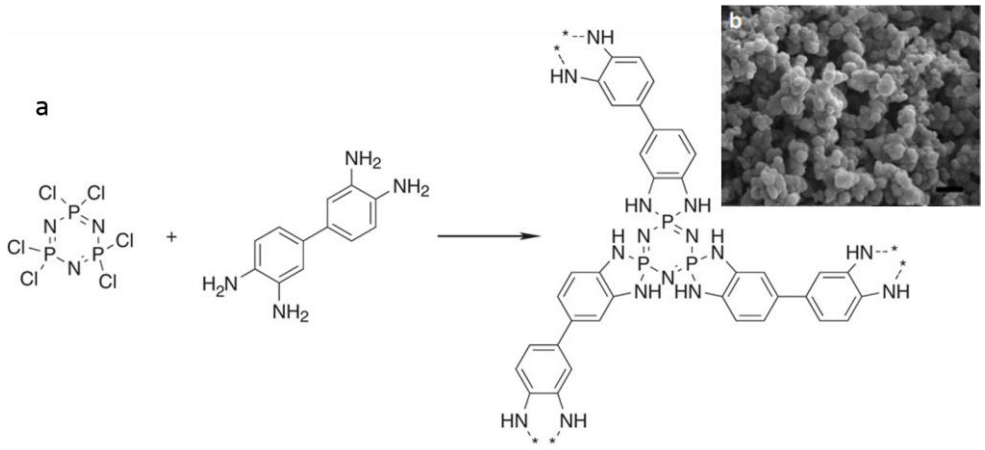

Fig. 13 (a) Reaction scheme for the synthesis of PECONFs, and (b) SEM shows the intergrown spherical macroporosity. [63]

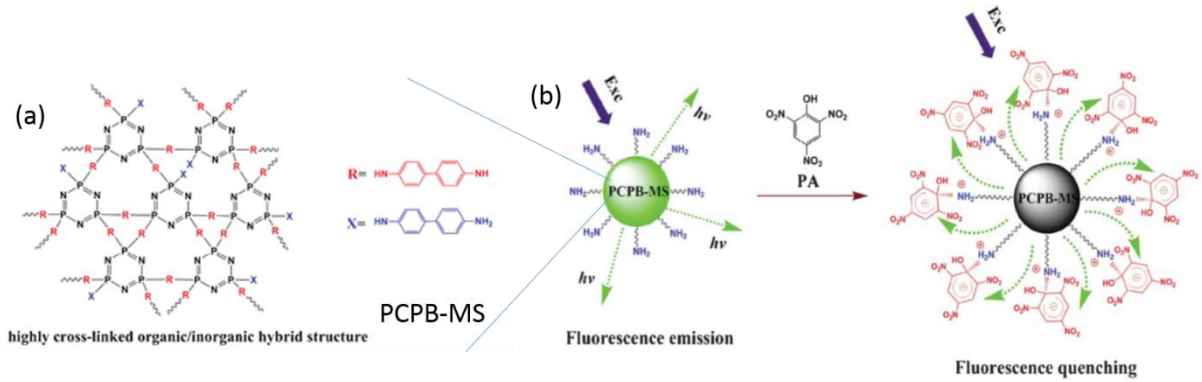

Fig. 14 (a) Molecular structure of PCPB-MS, and (b) fluorescence quenching detection of PA with PCPB-MS based on resonance energy transfer mechanism. [50]

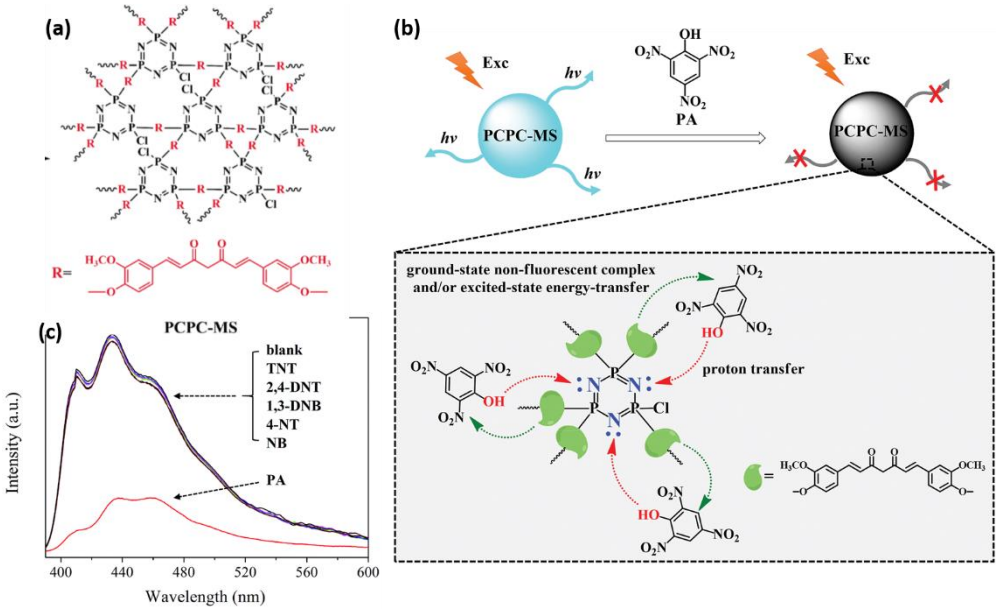

Fig. 15 (a) Chemical structure of PCPC-MS; (b) Fluorescence emission spectra of PCPC-MS in methanol. [56]

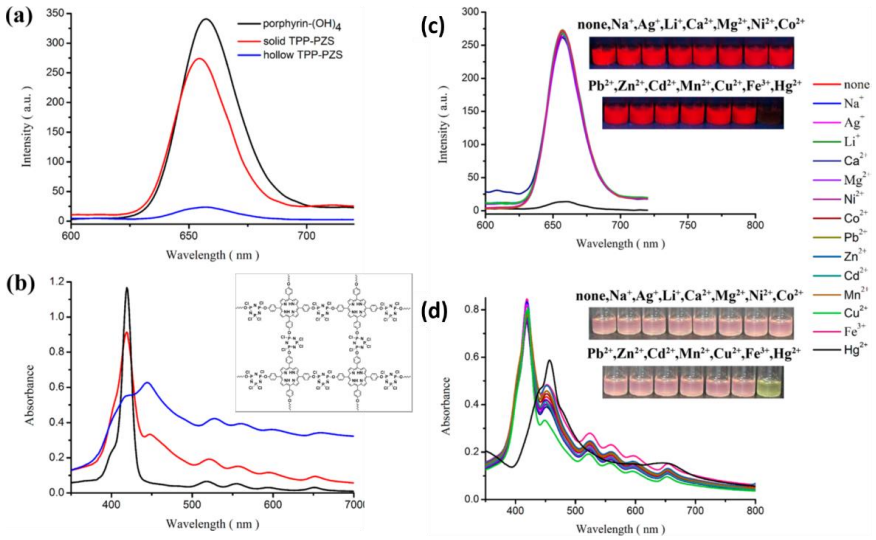

Fig. 16 (a) Fluorescence spectra and (b) UV-vis spectra of TPP-$(OH)_4$ solution (10 μM), solid TPP-PZS ($C_{porphyrin}$ = 9.7 μM) and hollow TPP-PZS ($C_{porphyrin}$ = 12.4 μM) suspension in ethanol. (c) UV-vis spectra (inset: photograph) and (d) fluorescence spectra (inset: fluorescence images) of solid TPP-PZS suspension (10 mg/l) in the absence and the presence of different metal ions (10 μM). The wavelength of exciting light is 365 nm. [55]

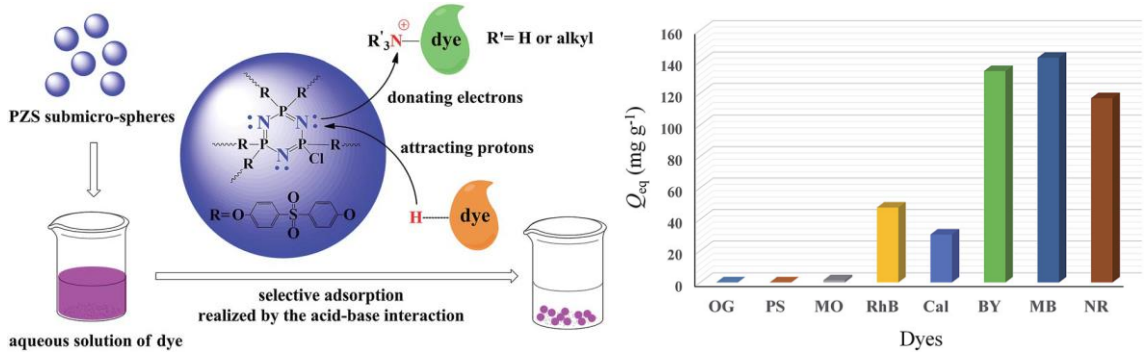

Fig. 17 Schematic representation of the selective adsorption of organic dyes in an aqueous solution by PZS based on acid-base interactions(left). Equilibrium adsorption capacities (Qeq) of PZS towards dyes at 25 °C(right). [91]

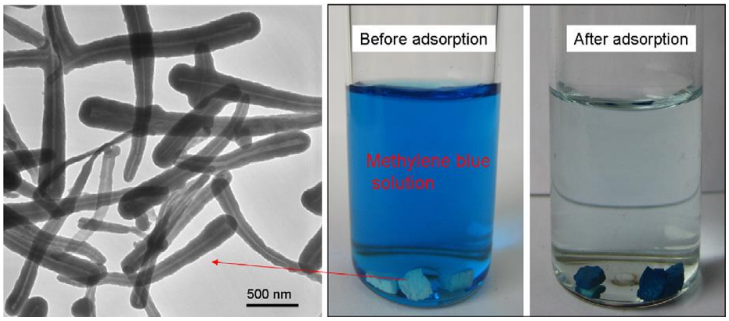

Fig. 18 PZS nanotubes and the adsorption test for MB (Conditions: 15 mg CPFs, pH 6.47, temperature 298 K, contact time 15 min). [93]

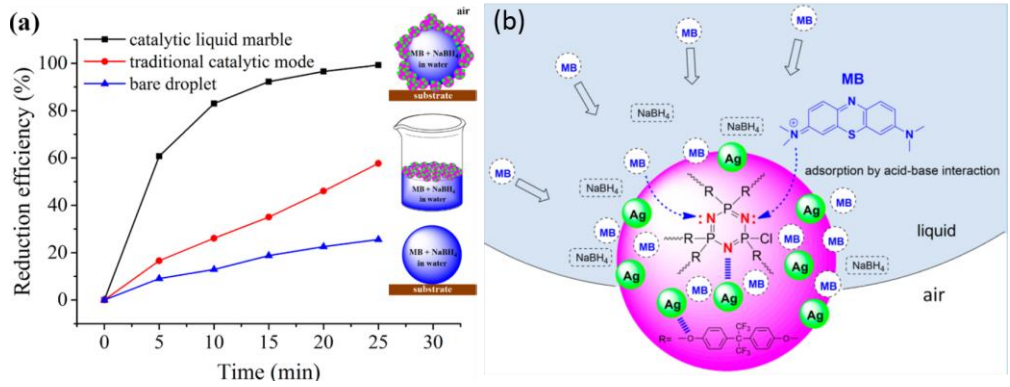

Fig. 19 (a) reduction kinetic curves and (b) illustration of the mass transfer of MB from bulk solution to the Ag catalytic active sites facilitated by the adsorption of MB onto PZAF particles via acid-base interactions. [53]

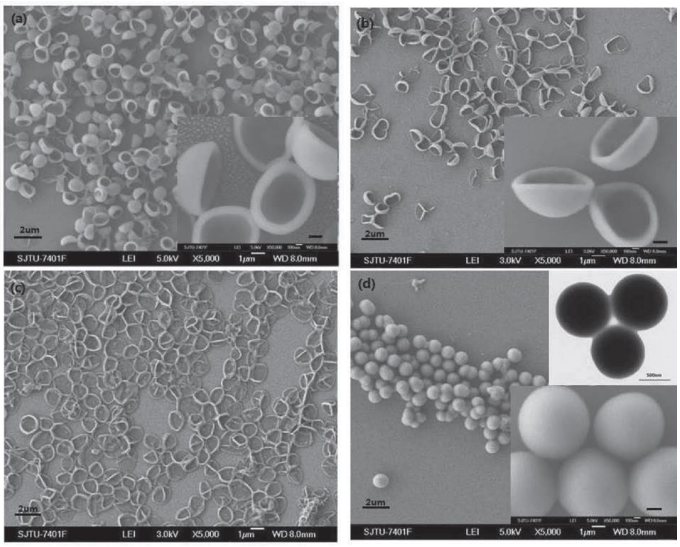

Fig. 20 SEM images of PCTP microspheres treated for 2 h with different solvents: a) acetone, b) THF, c) DMF, and d) deionized water (scale bar of insets in the lower right corner of (a, b, d) is 200 nm; the upper right corner in (d) is a TEM image of PCTP microspheres treated by deionized water, scale bar is 500 nm). [102]

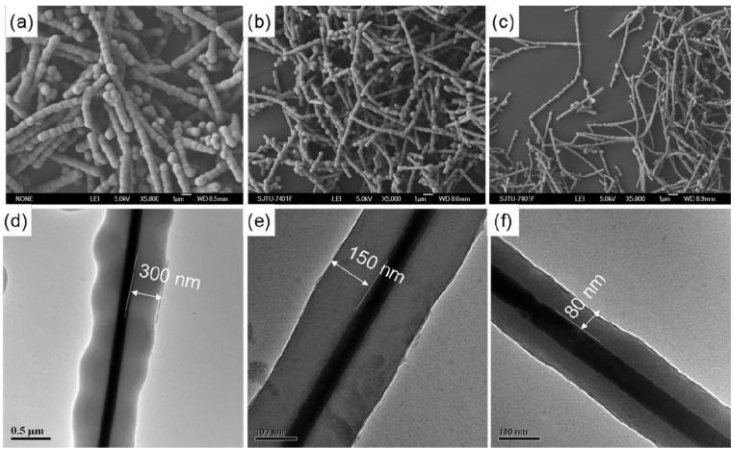

Fig. 21 SEM (a-c) and corresponding TEM (d-f) images of three types of silver/PZS nanocables with sheath thickness of ~300, ~150, and ~80 nm, respectively. The molar ratio of Ag:HCCP:BPS was 5:3:9 (a), 5:2:6 (b), and 5:1:3 (c), respectively. The sheath thickness of the nanocables can be controlled by the feed ratios. [79]

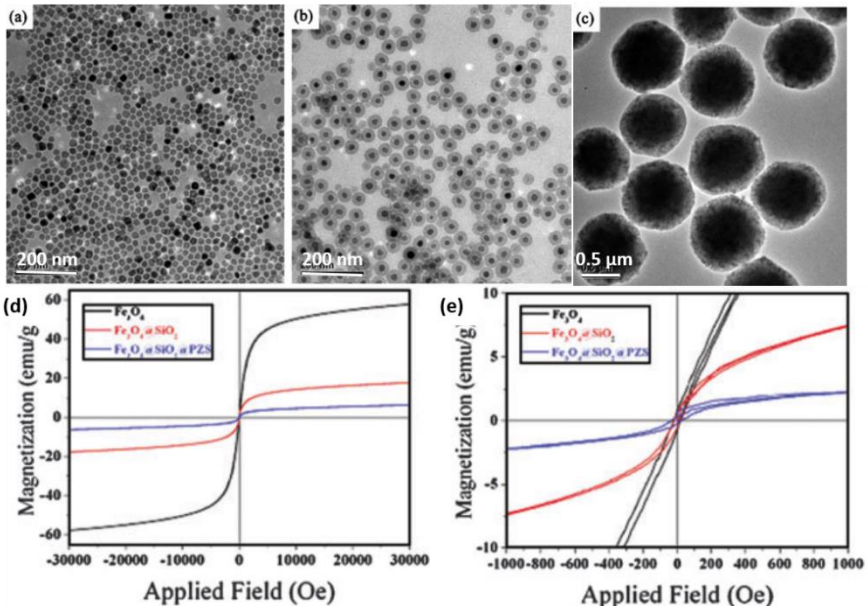

Fig. 22 TEM images of (a) Fe_3O_4, (b) Fe_3O_4@SiO_2, (c) Fe_3O_4@SiO_2@ PZS, and (d) The field dependent magnetization curve of the as-synthesized materials measured at 300 K, (e) magnified curve of the surrounding origin in (d).

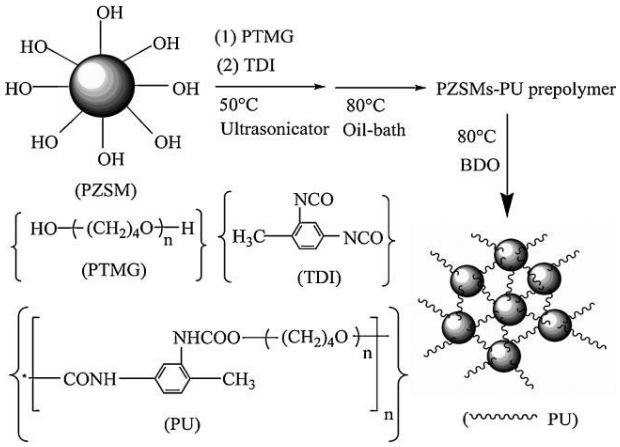

Fig. 23 Synthetic route for the fabrication of PU/PZS composite. [129]

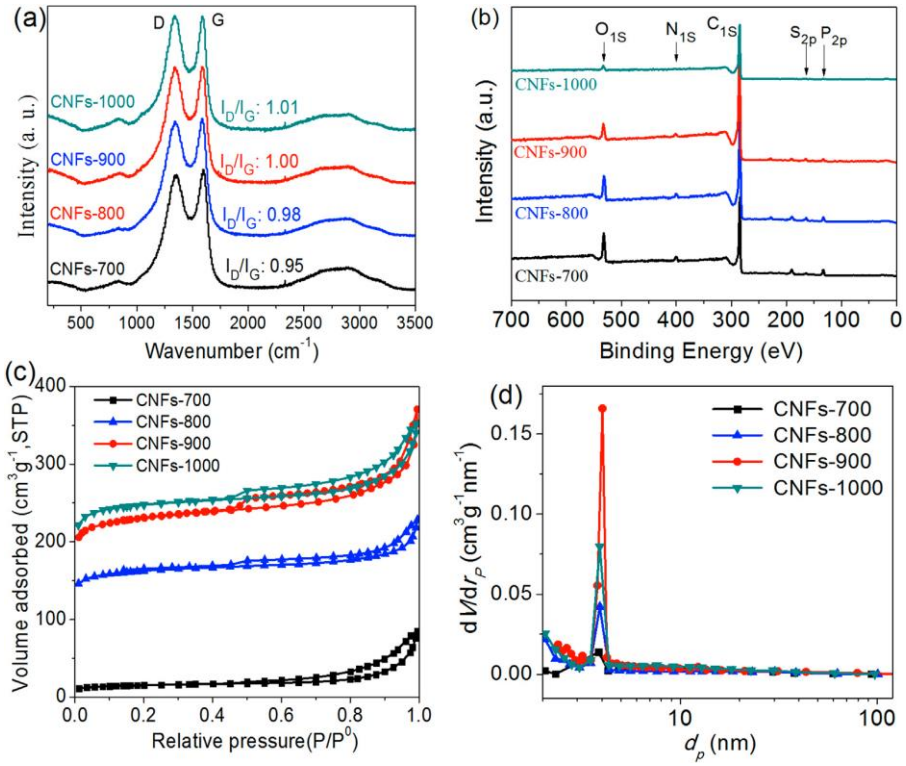

Fig. 24 (a) Raman spectra of HMCNTs. (b) Wide-survey XPS spectra of the HMCNTs. (c) Nitrogen adsorption-desorption isotherms and (d) pore size distribution curves of HMCNTs carbonized at various temperatures.[133]

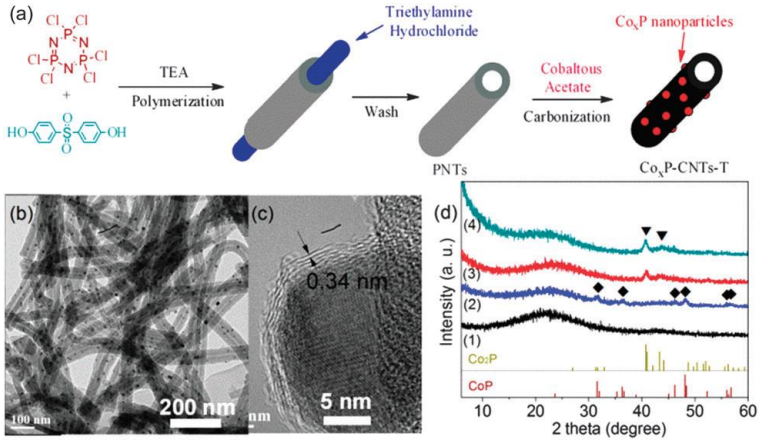

Fig. 25 (a) Synthesis scheme of heteroatoms-doped mesoporous CNTs loaded with Co_xP nanoparticles. (b) TEM image of Co_xP- CNTs -1000. (c) TEM image of a Co_xP nanoparticle embedded in graphitic carbon outer layers. (d) XRD patterns of Co_xP- CNTs -T, (1): Co_xP- CNTs -700, (2): Co_xP- CNTs -800, (3): Co_xP- CNTs -900, (4): Co_xP- CNTs -1000. ♦and ▼ are used to sign the XRD peaks of CoP and Co_2P, respectively.[139]

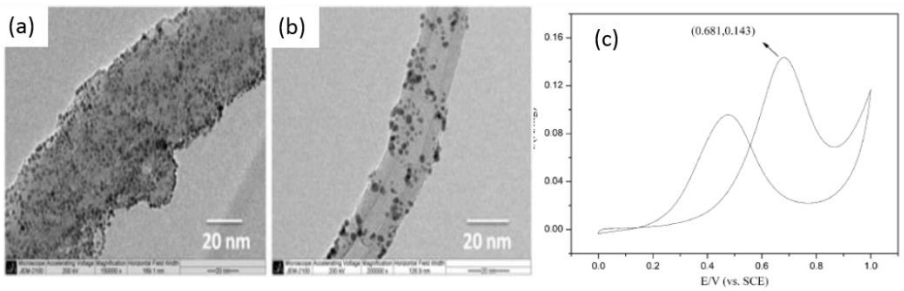

Fig. 26 TEM images of Pt nanoparticles loaded on the surface of (a) PZAF/CNTs and (b) pristine CNTs[140], (c) Cyclic voltammogram of Pt/PZAF/CNTs for methanol oxidation in 0.5M MeOH+0.5M H_2SO_4 at a scan rate of 50 mV s^{-1}.[140]

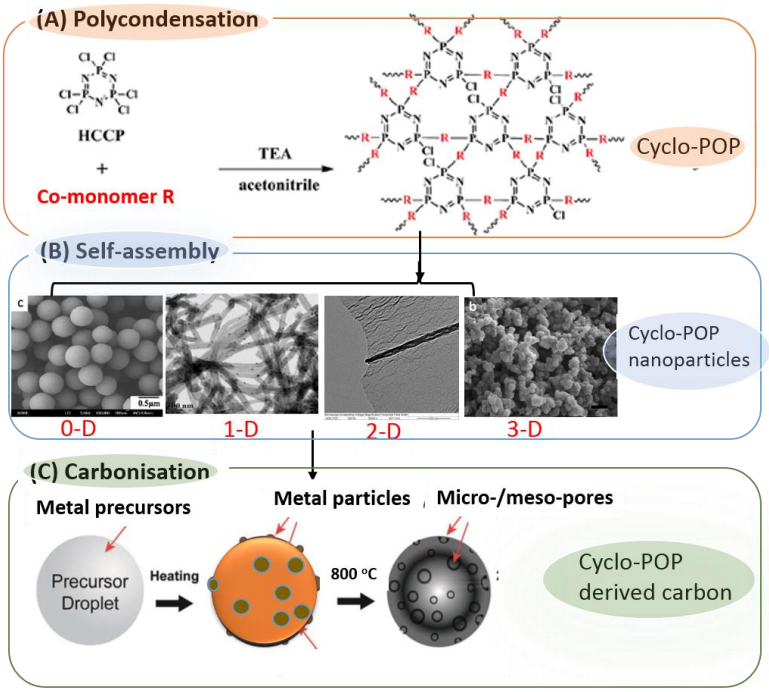

Fig.27 Synthesis of cyclo-POPs and the three stages of functionalization.

Table 1 Synthesis of cyclo-POPs particles with different morphology and geometries.

Co-monomers	Solvent	Reaction condition	CPFs dimensions
Micro/nanospheres			
4,4′-sulfonyldiphenol (BPS)[43] 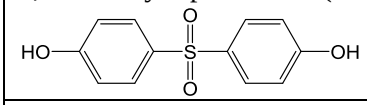	acetone	Sonication at room temperature for 3h	Microspheres, diameter (D) =1.24 ±0.08 μm
4,4'-Diaminodiphenyl ether (ODA)[44] 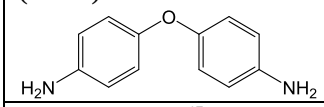	acetonitrile	Sonication at 40 °C for 4h	Microspheres, D=0.5~ 2.5 μm
trimethoprime[45] 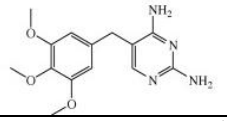	acetonitrile	sonication at 40 °C for 4h	Microspheres, D= 0.5~1.0 μm depends on the HCCP/TMP ratio
4-acetamidophenol[46] 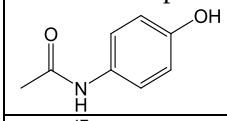	acetone containing K_2CO_3	Stirring at 70 °C for 24h under dry argon atmosphere	
BPS[47]	acetonitrile	sonication (100 W, 40 kHz) at room temperature for 5 h.	Mesoporous hollow spheres after removing the calcium carbonate (100~300 nm) as the core.
L-cystine methyl ester[48] 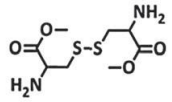	acetonitrile	HCCP/CysM=1/3 , stirring at room temperature for 48h	Spheres 250 nm ~2 μm, depending on HCCP concentration
(3,5-ditrifluoromethyl) phenylhydroquinone (6F-PH)[49] 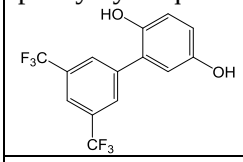	acetonitrile	HCCP/6F-PH=1/1, sonication at room temperature for 3h	Sphere size increases from 0.57, 0.69, 0.88, to 0.97 μm with increasing sonication power and HCCP concentration
Trimethoprim(TMP) [45] 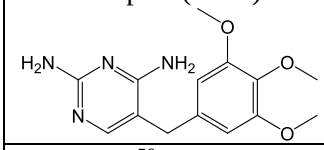	acetonitrile	TMP/HCCP =1/1~1/6, sonication at 40 °C for 4h	Microspheres size increases from 0.5 to 1.1 μm with increasing TMP concentration. Yield 79%
Benzidine[50] 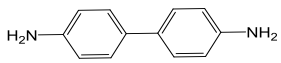	acetonitrile	Benzidine/HCCP =4/1, sonication at 45 °C for 48h in dark.	Microspheres of about 2.3 μm

Fluorescein[51] 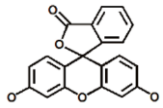	acetonitrile	Fluorescein/HCCP (3/1), sonication (100 W, 40 kHz) for 6 h at room temperature	With SiO_2 as a template, nanoshells contained ~2.2 nm mesopores
Phloroglucinol[52] 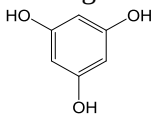	acetonitrile	phloroglucinol /HCCP (2/1), sonication ((150 W, 40 kHz) for 2 h at 30 °C	Microsphere size increases from 600 nm to 1.1 μm, with the concentration of HCCP increasing
Branched polyethylenimine[27] 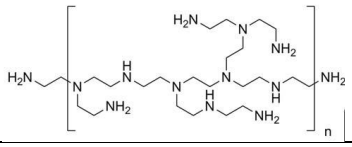	acetonitrile	PEI/HCCP=3/1 Sonication at 50 °C for 3h	D= 300 to 800 nm with increasing PEI content
4,4′-hexafluoroisopropylidene)diphenol (BPAF) [53] 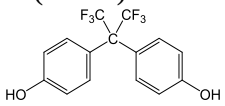	acetonitrile	BPAF/HCCP=1/3 mole, (200 W, 40 kHz) at about 50 °C for 5 h.	Ag doped microspheres used as stabilizer for formation of liquid marbles as catalytic miniature reactor
4,5-dibromofluorescein (DBF)[54] 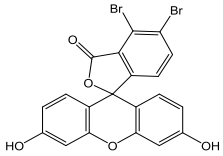	acetonitrile	DBF/HCCP=1.5/1 50 W, 40 kHz, room temperature, 3h	Spheres D=323 nm, high fluorescence, biocompatibility and improved resistance to photobleaching and protein interference.
5,10,15,20-tetrakis(4-hydroxyphenyl)porphyrin (TPP-(OH)$_4$)[55] 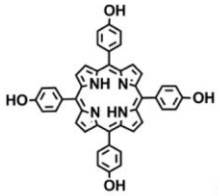	acetonitrile or acetone	50 W, 40 kHz for 0.5 h	Hollow spheres of about 246 nm formed in acetonitrile; and solid spheres of about 672 nm formed in acetone. The solid particles showed high fluorescence efficiency.
curcumin[56] 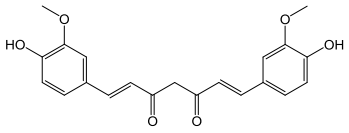	acetonitrile	Curcumin/HCCP =3/1 sonication (200 W, 40 kHz) at 40 °C for 7 h.	Spheres D= 1.0 μm.
Nanotubes			
BPS [35]	THF	Sonication (50 W, 40 Hz) at room temperature for 3h	Nanotubes: D=30-60, 1-2 μm in length

BPS[36]	THF	Sonication (50 W, 40 Hz) at 40 °C for 24h	Close-ended nanotubes, ~30 nm in inner diameter and ~100 nm in outer diameter, few micrometer in length
BPS[57]	THF	Sonication (50 W, 80 Hz) at room temperature for 2h, then add additional TEA, then for 10h	Branched nanotubes, close ended. Inner diameter 8nm, ~150 nm external diameter.
BPS[58]	acetone/toluene HCCP/BPS (1/3)	Magnetic stirring at room temperature for 5h.	capsicum-like nanotubes, close ended. Inner diameter 30-50 nm, 200~500 nm external diameter, 2~6 μm long.
BPS[59]	acetone	Sonication at room temperature for 3h	Nanofibres, 20~50 nm in diameter and 500 nm
BPS[36]	acetone	Stirring at room temperature for 3h	hexagonal shaped microtubes D=1~3 μm, wall thickness of 200-500 nm, length 100 μm
BPS[60]	acetone	Sonication at 7 °C for 10 min, yield 75%	Nanofibers diameter of 40~60 nm and length up to several micrometers long. BET surface area 70.3 m^2/g
Nanosheets			
p-Phenylenediamine[61] 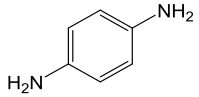	THF	HCCP/PDA (1/3), hydrothermal 393K 24h	Sheet-like structure, specific surface area 27.2 m^2/g, total pore volume 0.077 cm^3/g, pore size 1~2 nm.
melamine [62] 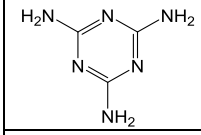	DMF	sonication at room temperature for 48h	0.91 nm in thickness with layer spacing of about 9 nm
Monolith			
3,3′-diaminobenzidine (DAB) [63] 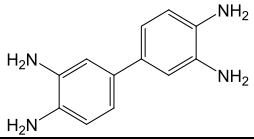	dimethylsulphoxide (DMSO)		Agglomerates of spheres of average diameter ranging from 600, 400 to 200 nm

Table 2 Comparison of saturation adsorption capacities for MB by different adsorbents at 298 K and pH ~7. [93]

Adsorbents	Adsorption capacity (mg/g)
CNTs [95]	35.4
Magnetite loaded MWCNTs [96]	48.06
Zeolite [97]	10.86
Polyurethane foam [98]	23.03
Polyaniline nanotubes base/silica composites [99]	5.38
Polyaniline nanotubes [100]	4.8
CPF nanotubes [93]	69.16